



## THESIS APPROVAL SHEET

Title of Thesis: Effective Emissivity of Nonisothermal Isogrid for Spacecraft Radiator Applications

Name of Candidate: Seth Abramczyk  
Master of Science 2021  
Graduate Program: MS-MENG

Thesis and Abstract Approved:

*Ruey-Hung Chen*

Ruey-Hung Chen  
Mechanical Engineering  
COEIT  
11/29/2021 | 11:12:02 AM EST

NOTE: \*The Approval Sheet with the original signature must accompany the thesis or dissertation. No terminal punctuation is to be used.

## ABSTRACT

Title of Document:

### EFFECTIVE EMISSIVITY OF NONISOTHERMAL ISOGRID FOR SPACECRAFT RADIATOR APPLICATIONS

Seth Abramczyk, Master of Science, 2021

Directed By:

Dr. Ruey-Hung Chen, Professor and Chair,  
Department of Mechanical Engineering

Accurate knowledge of the optical properties of spacecraft components, especially external components, is critical for proper spacecraft thermal design. The effective emissivity of isogrid (an array of equilateral triangular cavities) is not well understood, which poses a challenge for spacecraft thermal management. In this thesis the effective emissivity of isogrid with a prescribed base temperature and nonisothermal walls is examined. The temperature profile of the cavity's walls and the overall effective emissivity of the cavity are found using Thermal Desktop with Monte Carlo ray tracing. The effective emissivity's dependence on the wall height, wall thickness, wall resistance, and surface emissivity are examined. The existence of a critical wall height, and the contributing factors to this critical height, are discussed. Comparisons between isogrid and cavities with different base geometries are made. A variable emissivity isogrid spacecraft radiator concept employing the cavity effect is proposed, and mechanisms for achieving this are discussed.

EFFECTIVE EMISSIVITY OF NONISOTHERMAL ISOGRID FOR  
SPACECRAFT RADIATOR APPLICATIONS

By

Seth Aaron Abramczyk

Thesis submitted to the Faculty of the Graduate School of the  
University of Maryland, Baltimore County, in partial fulfillment  
of the requirements for the degree of  
Master of Science  
2021

© Copyright by  
Seth Aaron Abramczyk  
2021



## Dedication

In the hopes that this work may in some way contribute to their exploration of space, this is dedicated to the crew members of this country's present and future manned space programs. If only I could join them in their exciting endeavors!

- Dedication from Edwin "Buzz" Aldrin's Ph.D. Dissertation, 1963

## Acknowledgements

I'd first like to thank Dr. Ruey-Hung Chen for all of his help and support in writing this thesis. Dr. Chen dedicated a large amount of time meeting with me every week and providing extremely helpful feedback and edits on drafts of this thesis.

I'd like to thank Dr. Vivek Dwivedi for encouraging me to research this topic in the first place. Vivek has helped me every step of the way for the past two years that I've been working on this project. This thesis topic simply could not have happened without him.

Thank you especially to John Hawk, Rob Chalmers, and everyone involved in the Roman Space Telescope project. RST was the original impetus for this work, and John allowed me to spend RST time working on this thesis, for which I am eternally grateful.

Thank you to my cat, Tex, for never allowing me to work uninterrupted for more than an hour at a time. Last but certainly not least I'd like to thank my entire family for their love and support during my educational career. It's been a winding and at times bumpy road, and I am truly grateful for their support every step of the way.

# Table of Contents

Dedication.....	II
Acknowledgements.....	III
Table of Contents.....	IV
List of Tables.....	VI
List of Figures.....	VII
Nomenclature.....	VIII
Chapter 1: Background.....	1
1.1. Effective Emissivity and the Cavity Effect.....	1
1.2. Spacecraft Thermal Control Overview.....	2
1.2.1. Spacecraft Thermal Environment.....	2
1.2.2. Thermal Control Coatings.....	5
1.2.3. Active vs. Passive Thermal Control.....	6
1.3. Motivation.....	7
1.3.1. Variable Emissivity Devices.....	7
1.3.2. Nancy Grace Roman Space Telescope.....	10
Chapter 2: Methodology.....	13
2.1. Analytical Formulation & Problem Description.....	13
2.1.1. Problem Description.....	13
2.1.2. Coordinate System.....	13
2.1.3. Assumptions.....	14
2.1.4. Governing Equations.....	16
2.2. Thermal Desktop.....	21
2.2.1. Background.....	21
2.2.2. RadCAD.....	22
2.2.3. SINDA.....	25
2.3. Thermal Desktop Final Mathematical Formulation.....	29
2.4. Thermal Desktop Isogrid Model.....	31
2.4.1. Determining Appropriate Isogrid Array Size.....	31
2.4.2. Isogrid Model Overview.....	33
2.4.3. Effect of the Wall Nodalization on $\epsilon_{eff}$ .....	34
Chapter 3: Results.....	36
3.1. Model Parameters.....	36
3.1.1. Nondimensional Wall Height ( $\eta$ ).....	36
3.1.2. Nondimensional Wall Thickness ( $\lambda$ ).....	37
3.1.3. Characteristic Wall Resistance ( $R_{char}$ ).....	37
3.1.4. Base Temperature ( $T_b$ ).....	38
3.2. View Factors Across Surface 1.....	38
3.3. Temperature Profile.....	39
3.4. Effect of Varying Wall Height ( $\eta$ ).....	42
3.4.1. Characteristic $\epsilon_{eff}$ vs $\eta$ .....	42
3.4.2. Results of $\epsilon_{eff}$ vs $\eta$ .....	44
3.4.3. Contributions to the Critical Wall Height.....	46
3.4.4. Isothermal vs Nonisothermal Cavity Walls.....	48

3.5.	Effect of Varying Wall Thickness ( $\lambda$ ).....	49
3.5.1.	Results of Varying Wall Thickness ( $\lambda$ ).....	49
3.6.	Effect of Varying Characteristic Wall Resistance ( $R_{char}$ ) .....	50
3.7.	Edge Effects .....	51
3.8.	Isogrid vs. Other Geometries .....	54
Chapter 4: Variable Emissivity Isogrid Radiator Concept .....		58
4.1.	Description.....	58
4.2.	Variable Emissivity Actuation Methods.....	58
4.2.1.	Variable Base .....	58
4.2.2.	Variable Walls .....	60
Chapter 5: Summary and Future Work.....		62
5.1.	Conclusion .....	62
5.2.	Future Work .....	63
Bibliography .....		66

## List of Tables

Table 1: Textbook vs RadCAD View Factor Comparison Results .....	24
Table 2: Characteristic Regions Tabulated Values .....	44

## List of Figures

Figure 1: $\alpha$ and $\varepsilon$ of Various Surface Finishes [5].....	6
Figure 2: Louver Assembly Schematic [5] .....	9
Figure 3: Roman Space Telescope Thermal Model [20].....	11
Figure 4: Coordinate System for the Isogrid and Designation of Its surfaces .....	13
Figure 5: Finite Difference Formulation on Surface 1 [1].....	18
Figure 6: View Factor Between Two Finite Areas [23] .....	19
Figure 7: Orbit in Thermal Desktop [25].....	22
Figure 8: Geometry 1 View Factor [23] .....	23
Figure 9: Geometry 2 View Factor [23] .....	24
Figure 10: Geometry 3 View Factor [23] .....	24
Figure 11: Example Problem 1 Description [1].....	26
Figure 12: Example Problem 1 Thermal Desktop Model.....	26
Figure 13: Example Problem 1 Solution [1].....	27
Figure 14: Example Problem 2 Description [1].....	28
Figure 15: Example Problem 2 Thermal Desktop Temperature Profile .....	28
Figure 16: Example Problem 2 Thermal Desktop Solution.....	29
Figure 17: Varying Rectangular Isogrid Array Size .....	32
Figure 18: Center Cell $\varepsilon_{eff}$ for Varying Array Size .....	33
Figure 19: Thermal Desktop Isogrid Array Model.....	34
Figure 20: View Factors Across Surface 1 for $\eta=3.46$ .....	39
Figure 21: $F1 - Space$ Across $z$ for $\eta = 3.46$ .....	39
Figure 22: $\Delta T$ Temperature Profile for $\varepsilon_{surf} = 0.7, \eta = 3.46, \lambda = 0.010$ .....	40
Figure 23: $\Delta T$ Temperature Profile Across $z$ for $\varepsilon_{surf} = 0.7, \eta = 3.46, \lambda = 0.010$ ....	40
Figure 24: $\Delta T$ Temperature Profile Across $x$ for $\varepsilon_{surf} = 0.7, \eta = 3.46, \lambda = 0.010$ ....	41
Figure 25: Maximum $\Delta T$ vs $\eta$ for $\varepsilon_{surf} = 0.7, \lambda = 0.010$ .....	42
Figure 26: Characteristic Regions of $\varepsilon_{eff}$ vs $\eta$ .....	43
Figure 27: $\varepsilon_{eff}$ vs $\eta$ for Various $\varepsilon_{surf}$ and $\lambda = 0.010$ .....	44
Figure 28: $\varepsilon_{eff}/\varepsilon_{surf}$ vs $\eta$ for Various $\varepsilon_{surf}$ and $\lambda = 0.010$ .....	45
Figure 29: Contributing Factors to $\eta_{crit}$ for $\varepsilon_{surf} = 0.7$ and $\lambda = 0.010$ .....	47
Figure 30: Isothermal vs Nonisothermal $\varepsilon_{eff}$ for $\lambda = 0.010$ .....	49
Figure 31: Varying Nodalization for $\eta = 0.010$ .....	35
Figure 32: $\varepsilon_{eff}$ vs $\eta$ for Various $\lambda$ .....	50
Figure 33: $\varepsilon_{eff}$ vs $R_{char}$ for Various $\varepsilon_{surf}$ .....	51
Figure 34: Isogrid Array .....	52
Figure 35: Cavity Array Edge Effect in the X Direction .....	52
Figure 36: Cavity Array Edge Effect in the Y Direction .....	53
Figure 37: Different Cavity Geometries Tested.....	54
Figure 38: $\varepsilon_{eff}$ vs $\eta$ for Single Cell of Different Geometries .....	55
Figure 39: Perimeter to Area Ratio for Various Shapes .....	56
Figure 40: Constant Walls & Variable Base Radiator Schematic .....	59
Figure 41: Constant Base and Variable Walls “Propeller” Radiator Schematic .....	60

## Nomenclature

<u>Latin Symbol</u>	<u>Units</u>	<u>Description</u>
$A$	$m^2$	Surface area
$C_p$	$\frac{J}{kg * K}$	Specific heat capacity
$F_{j-k}$		View factor from $j$ to $k$
$H$	$m$	Wall height
$k$	$\frac{W}{m * K}$	Thermal conductivity
$L$	$m$	Wall length
$Q$	$W$	Heat rate
$Q_{j-k}$	$W$	Heat rate from $j$ to $k$
$q''$	$\frac{W}{m^2}$	Surface heat flux
$q'''$	$\frac{W}{m^3}$	Volumetric heat generation rate
$R_{char}$	$K/W$	Characteristic Resistance
$T$	$K$	Temperature
$t$	$m$	Wall thickness
<u>Greek Symbol</u>	<u>Units</u>	<u>Description</u>
$\alpha$		Solar absorptivity
$\varepsilon$		Infrared emissivity
$\varepsilon_{eff}$		Effective infrared emissivity

$\varepsilon_{eff\ max}$		Maximum effective infrared emissivity
$\varepsilon_j$		Surface infrared emissivity at j
$\varepsilon_{surf}$		Surface infrared emissivity
		Nondimensionalized height
$\eta$		$\eta = \frac{A_{walls}}{A_{base}} = \frac{12H}{\sqrt{3}L}$
$\eta_{crit}$		Critical wall height
$\eta_{equiv}$		Wall height equivalent to a flat plate
		Nondimensionalized wall thickness
$\lambda$		$\lambda = \frac{t}{L}$
$\rho$	$\frac{kg}{m^3}$	Density
$\sigma$	$5.67 \times 10^{-8} \frac{W}{m^2 * K^4}$	Stefan–Boltzmann constant

# Chapter 1: Background

## 1.1. Effective Emissivity and the Cavity Effect

The emissivity ( $\epsilon$ ) of a surface for a given wavelength “provides a measure of how efficiently [the] surface emits energy relative to a blackbody” [1]. The effective emissivity ( $\epsilon_{eff}$ ) can be defined for a cavity as the “ratio of the radiant power leaving the cavity to that from a blackbody having the area of the cavity opening and a temperature of the inner surfaces of the cavity” [1]. The “effective” emissivity is not necessarily the same value as the surface emissivity ( $\epsilon_{surf}$ ) of the cavity’s walls, but rather is the emissivity of the cavity as a whole. The cavity effect has been well studied, and is used in the field of radiation thermometry in order to closely approximate a blackbody for calibration purposes [2]. Its cause can be explained simply as being due to having an increased surface area from which to radiate when compared to that of a flat surface.

Much of the literature on the cavity effect has the assumption of isothermal cavities. This assumption may be valid for terrestrial radiation thermometry applications but is not necessarily a valid assumption for space radiator applications when the cavity is sufficiently deep and the temperature gradient between the base and opening of the cavity is non-trivial. Research into nonisothermal cavity walls tends to focus on temperature profiles prescribed by the authors rather than on solving for both the  $\epsilon_{eff}$  and temperature profiles simultaneously [3][4]. Most of the previous studies have focused on a single cavity rather than an array of cavities interacting with each other. While most other studies focus on cylindrical cavities, this is the first study to look specifically at isogrid (equilateral triangular cavities).

## 1.2. Spacecraft Thermal Control Overview

### 1.2.1. Spacecraft Thermal Environment

The spacecraft thermal environment is one of extremes. While the extremely thin atmosphere of low Earth orbit does cause drag on the spacecraft, it is negligible from a thermal perspective. Therefore, it is assumed in most cases that there is no convective heat transfer between the spacecraft and the environment, and all heat exchange is done via radiation.

This radiative exchange comes from several environmental sources. First, there is direct solar radiation from The Sun in the ultraviolet band. Unshielded from the Earth's atmosphere, this heat load ranges between approximately 1322 and 1414  $\frac{W}{m^2}$  [5]. The Sun's rays also bounce off The Earth which then impinge upon the spacecraft, known as albedo. The Earth emits infrared radiation which adds a heat load of approximately 150 to 250  $\frac{W}{m^2}$  [5] depending on the orbit. The steady state energy balance for a spacecraft is the sum of the environmental and internal heat loads. This summation equals the heat rejected to space, as shown below.

$$Q_{emitted} = Q_{solar} + Q_{albedo} + Q_{IR} + Q_{int} \quad (1)$$

$$A\varepsilon\sigma T^4 = A\alpha(q''_{solar} + q''_{albedo}) + A\varepsilon q''_{IR} + Q_{int} \quad (2) \quad [5]$$

Where  $Q_{solar}$ ,  $Q_{albedo}$ ,  $Q_{IR}$ , and  $Q_{int}$  are heat loads from the Sun, Earth albedo, Earth IR, and internal spacecraft components.  $A$  is the radiator area,  $\varepsilon$  is the IR emissivity,  $\alpha$  is the solar absorptivity,  $\sigma$  is the Stefan-Boltzmann constant, and  $T$  is the absolute temperature. Note that  $Q_{solar}$  and  $Q_{albedo}$  depend on  $\alpha$ , while the  $Q_{emitted}$  and  $Q_{IR}$  depend on  $\varepsilon$ .

### 1.2.1.1. *Radiators*

All spacecraft components which consume electrical power will dissipate waste heat through their operation. This waste heat is transported (either actively or passively) to specialized spacecraft surfaces called radiators, which then rejects the waste heat to space via radiative heat transfer.

For simplicity, let us assume a radiator only has radiative exchange with space and does not “see” The Sun, Earth, other spacecraft components, etc. These additional heat loads are known as backloads and are extremely common in real-world situations. With the assumption of no backloading, the heat emitted from the radiator is therefore given a modified version of eq (2), shown below.

$$Q = A\varepsilon\sigma T^4 \quad (3) \quad [5]$$

The radiator temperature is usually dependent on the requirements of other spacecraft components, and the operational temperature range of the radiator itself. Therefore, the thermal engineer is left with only the radiator area and emissivity as variables which may be changed to fit the design requirements. It is desirable from a mass and power perspective to size the radiator to be as small as possible. Radiator coatings are generally chosen to have a high IR emissivity (to dissipate more heat) and a low solar absorptivity (to reduce backloading on the radiator). Such coatings are discussed further in section 1.2.2.

### 1.2.1.2. *Radiator Sizing Example*

Let us assume that there is an electronics box located on a radiator which may dissipate between 10W and 50W of heat, depending on its power state. We will further make the simplifications that the radiator is isothermal, conductively isolated from the rest of the spacecraft, and does not receive any radiative backloading from The Sun, Earth, or

other spacecraft components or structures. The radiator has an upper temperature limit of 40°C, lower limit of -10°C, and has a surface emissivity of 0.9. For simplicity we will also assume that the temperature of space  $T_{space} = 0K$ .

Using this information, the task at hand is to determine the *minimum* radiator surface area required so as not to break the upper temperature limit when it is dissipating the maximum 50W of heat.

$$A = \frac{Q_{max}}{\varepsilon\sigma T_{max}^4}$$

$$A = \frac{50W}{(0.9) \left(5.67 * 10^{-8} \frac{W}{m^2K^4}\right) (40^\circ C + 273.15)^4} = 0.102m^2 \quad (4)$$

Using eq (4) the minimum required radiator area to maintain the 40°C upper limit is found to be 0.102 m<sup>2</sup>. Making the radiator any smaller will result in breaking the upper temperature limit.

Now suppose that the electronics box is turned to a low-power state and dissipates its minimum amount of heat, only 10W.

$$T = \left[ \frac{Q_{min}}{A\varepsilon\sigma} \right]^{\frac{1}{4}}$$

$$T = \left[ \frac{10W}{(0.102m^2)(0.9) \left(5.67 * 10^{-8} \frac{W}{m^2K^4}\right)} \right]^{\frac{1}{4}} = -63.7^\circ C \quad (5)$$

In this case, the resulting radiator temperature is only -63.7°C, well below the -10°C lower temperature limit. Decreasing the radiator area is not an option because, as found in eq (4), 0.102m<sup>2</sup> is the minimum area required to maintain the upper temperature limit. The only design solution we now have in order to not break the lower temperature limit is to place a heater on the radiator. This is known as a makeup heater, because it “makes up” the needed

heat to maintain the lower temperature limit. We may find the necessary size of this makeup heater by adding a  $Q_{heater}$  term in eq (3) below.

$$Q_{heater} = A\varepsilon\sigma T_{min}^4 - Q_{min}$$

$$Q_{heater} = (0.102m^2)(0.9) \left( 5.67 * 10^{-8} \frac{W}{m^2K^4} \right) (-10^\circ C + 273.15)^4 \quad (6)$$

$$- 10W = 14.9W$$

We find the required size of the makeup heater to be 14.9W. The design philosophy employed in sizing a radiator area is called cold-biasing [6]. In a cold-biased design, the radiator is sized to be large enough as to not break its upper temperature limit, and makeup heaters are used to break the cold limit.

### 1.2.2. Thermal Control Coatings

An important note is that in the world of spacecraft thermal engineering,  $\varepsilon$  refers specifically to the emissivity in the IR band (5 $\mu$ m - 100  $\mu$ m) [7]. The absorptivity ( $\alpha$ ) refers specifically to the absorptivity of incident radiation from The Sun (0.25 $\mu$ m - 2.8 $\mu$ m) [7]. Both  $\alpha$  and  $\varepsilon$  are measures of a surface's total hemispherical emissivity over their respective wavelengths.

As was shown in eq (2) the values  $\alpha$  and  $\varepsilon$  are of great importance in determining the surface's energy balance and thus its equilibrium temperature. Careful consideration must therefore be taken when choosing a surface finish. To that end, myriad thermal control coatings with a wide range of  $\alpha$  and  $\varepsilon$  properties have been developed. Values for various types of surface finishes and coatings are shown in Figure 1 below.

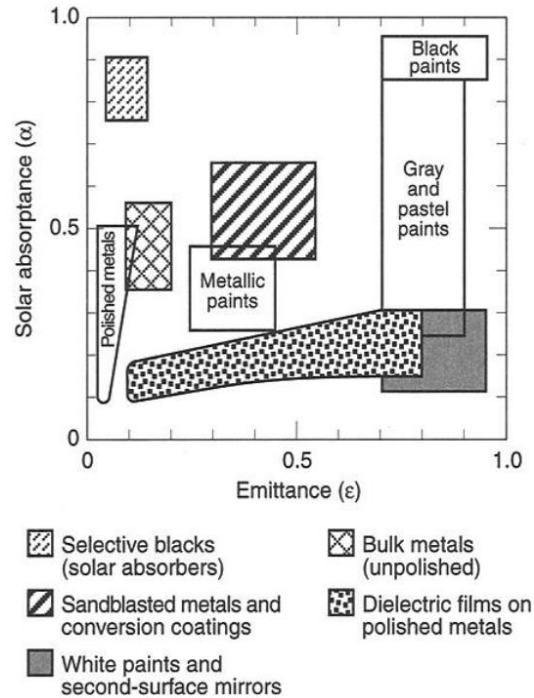


Figure 1:  $\alpha$  and  $\epsilon$  of Various Surface Finishes [5]

For the example of a radiator surface, it is desirable to have a high  $\epsilon$  to dissipate more heat, and a low  $\alpha$  as to decrease the solar loading. Therefore, radiators are typically coated with a diffuse white paint or have a specular mirrored finish. Special care must be taken for cryogenic components as  $\alpha$  and  $\epsilon$  vary at extreme temperatures.

### 1.2.3. Active vs. Passive Thermal Control

Passive thermal control refers specifically to spacecraft thermal control devices which do not require any additional spacecraft resources such as power to operate. They also do not change properties (such as emissivity) and have no moving parts [8]. The most common example of passive thermal control would be a thermal control coating with a specifically chosen  $\alpha$  and  $\epsilon$  value.

Unlike passive control, active thermal control devices do use spacecraft resources, such as power, change properties, and/or have moving parts [8]. The most common

example would be that of a heater, controlled either by a mechanical thermostat or via software control (typically P or PI control) [5].

Even though heat pipes have a working fluid which could be called a “moving part”, they are generally considered passive components because they do not require any additional spacecraft power to operate [5]. A pumped fluid loop is considered an active component because of the pump which drives the refrigeration cycle [5].

### 1.3. Motivation

#### 1.3.1. Variable Emissivity Devices

##### 1.3.1.1. Variable Emissivity Radiator Sizing Example

Let us revisit the radiator example from section 1.2.1.2. In that case the assumption was made that the radiator  $\epsilon$  was a constant value of 0.9. Suppose there was a method by which the emissivity could instead be varied. For the sake of argument, we will assume that the radiator’s emissivity varies linearly with temperature from a minimum value of 0.5 at  $-10^{\circ}\text{C}$  to a maximum of 0.9 at  $40^{\circ}\text{C}$ .

The hot case is the same as the previous example, as the radiator has a temperature of  $40^{\circ}\text{C}$  and an emissivity of 0.9. Using eq (3) we therefore find the area required as not to exceed this temperature to be  $0.102\text{ m}^2$ .

$$A = \frac{Q_{max}}{\epsilon_{max}\sigma T_{max}^4}$$

$$A = \frac{50W}{(0.9) \left(5.67 * 10^{-8} \frac{W}{m^2K^4}\right) (40^{\circ}\text{C} + 273.15)^4} = 0.102m^2 \quad (7)$$

For the cold case we assume that the electronics box enters a low-power state and dissipates only 10W. Using the calculated area of  $0.102 m^2$  and the minimum emissivity of 0.5, the resulting radiator temperature is  $-30.6^\circ\text{C}$ .

$$T = \left[ \frac{Q_{min}}{A\varepsilon_{min}\sigma} \right]^{\frac{1}{4}} \quad (8)$$

$$T = \left[ \frac{10W}{(0.102m^2)(0.5) \left( 5.67 * 10^{-8} \frac{W}{m^2K^4} \right)} \right]^{\frac{1}{4}} = -30.6^\circ\text{C}$$

This variable emissivity configuration now only requires a 3.6 W makeup heater to maintain the minimum temperature, compared to the 14.9 W makeup heater for the constant emissivity radiator.

$$Q_{heater} = A\varepsilon_{min}\sigma T_{min}^4 - Q_{min}$$

$$Q_{heater} = (0.102m^2)(0.5) \left( 5.67 * 10^{-8} \frac{W}{m^2K^4} \right) (-10^\circ\text{C} + 273.15)^4 - 10W = 3.6W \quad (9)$$

A power savings of 11.3 W might not sound like much, but on a spacecraft with a very tight power budget it can be a significant savings.

### 1.3.1.2. Thermal Control Louvers

A louver is a thermal control device designed to vary the effective IR emissivity ( $\varepsilon_{eff}$ ) and solar absorptivity ( $a_{eff}$ ) of a spacecraft's surface (usually an external radiator) based on the surface's temperature. A schematic of a typical louver is shown in Figure 2 below.

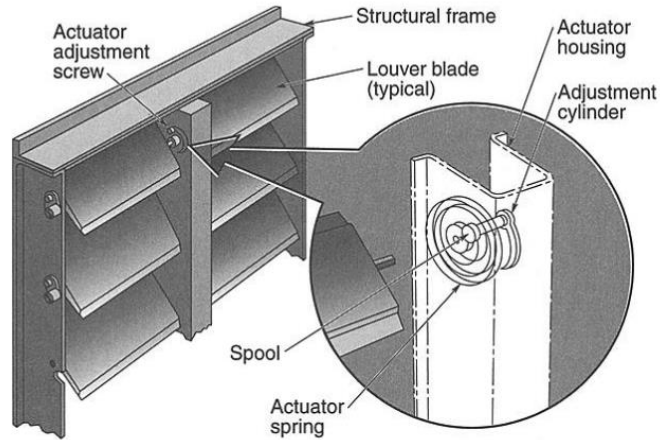


Figure 2: Louver Assembly Schematic [5]

The spacecraft surface covered by the louver is coated with a high- $\epsilon$  finish, and the exterior of each blade is coated to be low- $\epsilon$ . When the radiator surface is below the setpoint temperature, the blades remain closed causing the minimum amount of heat to escape into space. As the radiator temperature increases, bi-metallic strips on the sides of each blade expand and cause the blades to open. This gives the high- $\epsilon$  radiator surface a clearer view to space, significantly increasing the amount of heat rejected. As the radiator rejects more heat to space it begins to cool down. The lower temperature causes the bi-metallic strips to contract, closing the blades and decreasing the heat dissipation to space. The opening and closing of the blades serve to vary the system's effective emissivity to space. Careful tuning of the bi-metallic strips allow the radiator surface to maintain a desired setpoint temperature [5] with less need for makeup heaters.

### 1.3.1.3. *State of the Art Variable Emissivity Radiators*

Due primarily to their large mass, louvers are not used in industry as widely as they were several decades ago. An active area of research is focusing on miniaturizing the louver

to MEMS scales [9]–[11]. The most straightforward MEMS variable emissivity method is that of a MEMS louver. A MEMS louver would operate in much the same way as a traditional louver though at a fraction of the size, being only on the order of hundreds of microns in length [6].

Another method changes the geometry of the radiator to vary its view to space and thus its emissivity. While louvers maintain a constant area and vary the exposed surface emissivity, these radiators maintain a constant surface emissivity and vary the exposed area. This can be achieved through various methods including an accordion array of panels [12], origami inspired designs [13], and others [14]–[16].

A completely solid-state method uses electrochromic glass to expose and hide a mirrored surface sensitive to the IR band. “In the non-absorbing mode, light passes through the metamaterial top electrode and active element and is reflected back from the mirror electrode. When the system is activated to its absorbing mode by the application of a low voltage ( $\pm 1$  V) to the electrodes, the reflected light intensity diminishes and the system goes into a low-reflectance, high-emittance (High-  $\epsilon$ ) state. Reversing the electrode polarity brings the system back to a high-reflectance and low-emittance (Low-  $\epsilon$ ) state” [17].

### 1.3.2. Nancy Grace Roman Space Telescope

#### *1.3.2.1. Overview and Science Objectives*

The Nancy Grace Roman Space Telescope (RST), named after the “Mother of Hubble” [18], is one of NASA’s newest space telescopes. Set to launch in the mid-2020’s, RST will explore Dark Energy, Dark Matter, and Exoplanets [19]. RST was selected as the

top-ranked large space mission in the 2010 Astronomy and Astrophysics Decadal survey, and will orbit the second Earth-Sun Lagrange Point [20].

Of particular importance is the Wide Field Instrument (WFI), which is the main instrument on RST. It has the same resolution as the Hubble Space Telescope, but 100 times the field of view [21]. Over its first five years RST will image 50 times more of the sky than Hubble did over its first 30 years [21].

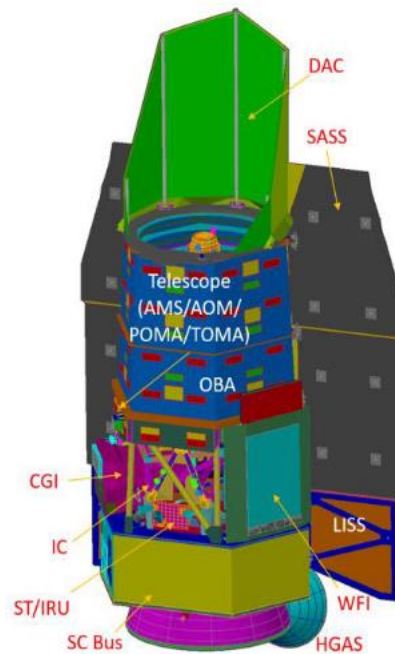


Figure 3: Roman Space Telescope Thermal Model [20]

The Coronagraph is the second instrument aboard RST. A coronagraph blots out the light from a star, allowing direct viewing of planets in its orbit. Through a complex array of masks, prisms, detectors, and self-flexing mirrors, RST will have the most sensitive coronagraph by several orders of magnitude [22].

### *1.3.2.2. Basic Thermal Design*

One of the most important components of RST's thermal design is the Solar Array/Sun Shield (SASS) which will both provide power to the spacecraft and block the payload from the Sun. The Lower Instrument Sun Shades (LISS) and the Deployable Aperture Cover (DAC) provide additional protection from solar impingement. The SASS, LISS, and DAC all help to provide a thermally stable environment for the spacecraft [20]. Because the WFI detects light in the IR band, the sensors must be maintained at cryogenic temperatures and extra care must be taken in the thermal design.

## Chapter 2: Methodology

### 2.1. Analytical Formulation & Problem Description

#### 2.1.1. Problem Description

Consider a single isogrid cavity within an arbitrarily large array of identical cavities. The array is sufficiently large so that we may examine a single cavity without needing to consider edge effects from the perimeter of the array. The base of the array is isothermal and set to some prescribed temperature. The array is in deep space, receiving no solar or IR irradiation from any source (Sun, Earth, etc.).

#### 2.1.2. Coordinate System

Let us define a cartesian coordinate system and cavity parameters as shown below in Figure 4.

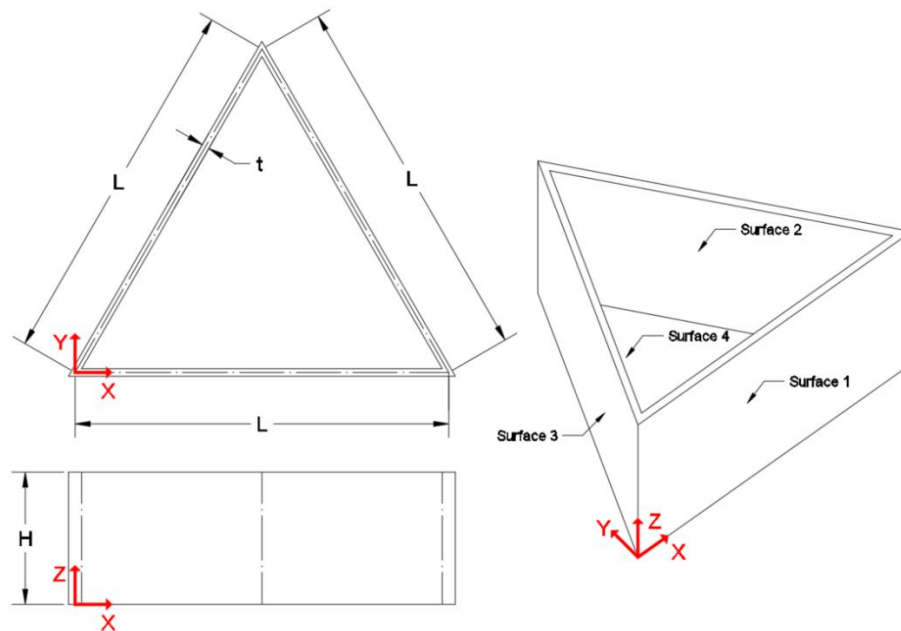


Figure 4: Coordinate System for the Isogrid and Designation of Its surfaces

In Figure 4,  $L$  is the side length,  $t$  is the wall thickness, and  $H$  is the cavity wall height. Note that the origin is located at the center of the wall, such that the inner face of surface 1 is located at  $y = t/2$ . The center of each surface is therefore defined by Eqn (10) below:

$$\begin{aligned}
 \text{Surface 1} & \begin{cases} 0 \leq x \leq L \\ y = 0 \\ 0 \leq z \leq H \end{cases} & \text{Surface 2} & \begin{cases} (L-x)\tan(60^\circ) = 0 \\ \frac{L}{2} \leq x \leq L \\ 0 \leq y \leq L\sin(60^\circ) \\ 0 \leq z \leq H \end{cases} \\
 \text{Surface 3} & \begin{cases} x\tan(60^\circ) = 0 \\ 0 \leq x \leq \frac{L}{2} \\ 0 \leq y \leq L\sin(60^\circ) \\ 0 \leq z \leq H \end{cases} & \text{Surface 4} & \begin{cases} 0 \leq x \leq L \\ 0 \leq y \leq x\tan(60^\circ); 0 \leq x \leq \frac{L}{2} \\ 0 \leq y \leq (L-x)\tan(60^\circ); \frac{L}{2} \leq x \leq L \\ z = 0 \end{cases}
 \end{aligned} \tag{10}$$

### 2.1.3. Assumptions

#### 2.1.3.1. General Assumptions

The following are assumptions and simplifications that will be used for the remainder of the analysis. The isogrid is assumed to be in the vacuum of space, and therefore there is no convective heat transfer with the environment. The isogrid cavity in question is a member of an arbitrarily large array of identical cavities with identical temperature profiles and material properties. Due to symmetry, it is assumed that the temperature profiles across surfaces 1, 2, and 3, as shown in Figure 4, are identical. The isogrid is assumed to be machined out of a solid piece of material, and as such there is no contact resistance between any of the surfaces. The isogrid material is assumed to have homogeneous, isotropic, and non-temperature dependent material properties. It is assumed to have been in its environment for a sufficiently long time such that the temperature profile has reached steady state and is not time varying. Assume that all surfaces are flat and therefore each of them has no direct view of itself. All surfaces are assumed to be diffuse and gray. Assume

no heat generation within the walls. The isogrid wall is assumed to be made of a thermally conductive material and have a sufficiently small thickness. We therefore assume that the temperature is constant through the wall thickness.

### 2.1.3.2. *Boundary Conditions*

Surface 4, the base of the isogrid, is assumed to be isothermal at temperature  $T_4$ , which is the temperature of the spacecraft surface whose temperature is to be controlled. Therefore, we can state that

$$T_n(x, y, 0) = T_4 \quad (11)$$

for surfaces  $n = 1, 2, 3$ . Space is equivalent to a concave black surface completely encompassing the isogrid with a temperature of 2.7 K. Due to symmetry, we assume that there is no heat conduction between the walls of the cavity, because they share the same temperature at the wall-wall interface.

$$\frac{\partial}{\partial x} T_1(0, 0, z) = \frac{\partial}{\partial x} T_1(L, 0, z) = 0 \quad (12)$$

Due to symmetry within each wall, we assume that the temperature profile of surface 1 is mirrored about the line  $x = \frac{L}{2}$ .

$$T_1(x, y, z) = T_1(L - x, y, z) \quad (13)$$

Due to this assumption, we may also say that

$$\frac{\partial}{\partial x} T_1\left(\frac{L}{2}, y, z\right) = 0 \quad (14)$$

#### 2.1.4. Governing Equations

Due to the assumption of symmetry, it is necessary only to calculate the temperature profile for surface 1. The temperatures of surfaces 2 and 3 are found by symmetry. Therefore, the following governing equations are only solved for surface 1.

##### 2.1.4.1. Analytical Formulation

The general 3D heat diffusion equation is

$$\rho C_p \frac{\partial T_1}{\partial t} = \frac{\partial}{\partial x} \left( k \frac{\partial T_1}{\partial x} \right) + \frac{\partial}{\partial y} \left( k \frac{\partial T_1}{\partial y} \right) + \frac{\partial}{\partial z} \left( k \frac{\partial T_1}{\partial z} \right) + q''' \quad (15) \quad [1]$$

where  $\rho$  is the density,  $C_p$  is the specific heat,  $k$  is the thermal conductivity,  $T_1$  is the temperature profile of surface 1, and  $q'''$  is the volumetric heat generation rate and  $q''' = 0$ .

Applying the assumptions of steady state conditions, homogeneous material properties with constant  $k$  independent of temperature, and no internal heat generation leads to this simplified version of Eqn (16).

$$k \left( \frac{\partial^2 T_1}{\partial x^2} + \frac{\partial^2 T_1}{\partial y^2} + \frac{\partial^2 T_1}{\partial z^2} \right) = 0 \quad (16) \quad [1]$$

From the assumptions stated earlier, the temperature through the thickness of the wall is isothermal, hence  $\frac{\partial T_1}{\partial y} = 0$ . If we insert  $\frac{\partial T_1}{\partial y} = 0$  into Eqn (16) the resulting formulation will be independent of  $y$  and thus independent of the wall thickness. However, in actuality the temperature profile *is* dependent on the wall thickness as will be described in section 3.3. Therefore, we must use a different formulation which maintains the temperature profile's dependence on the wall thickness.

#### 2.1.4.2. *Finite Difference Formulation*

To maintain the temperature dependence on the wall thickness we will use a finite difference approach. This is the formulation utilized by Thermal Desktop, which is discussed further in section 2.2.

Let us split surface 1 into an arbitrary number of elements in the  $x$  and  $z$  directions, with each element having thickness  $t$  in the  $y$  direction. Each element has a single node at its center and is assumed to be isothermal. In this way the  $\frac{\partial T_1}{\partial y} = 0$  condition is maintained by only having one control volume in the  $y$  direction, while simultaneously keeping the temperature dependent on  $t$ .

From the conservation of energy, steady state conditions, and lack of a convective environment, it is clear that for each element

$$Q_{net} = Q_{cond} + Q_{rad} = 0 \quad (17)$$

where  $Q_{net}$  is the net heat flow into the control volume,  $Q_{cond}$  is the heat flow due to conduction, and  $Q_{rad}$  is the heat flow from radiation.

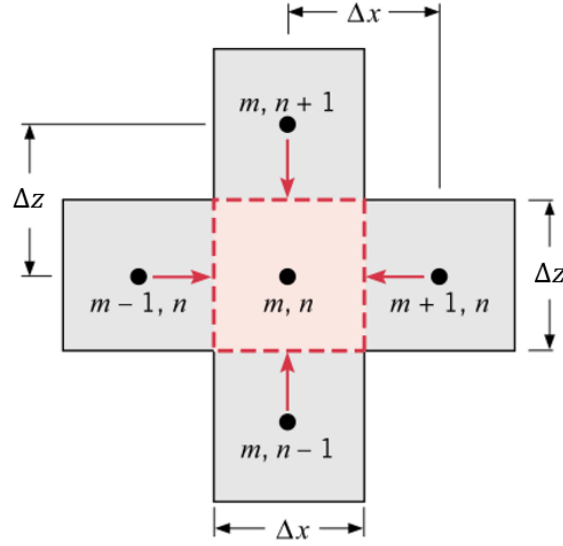


Figure 5: Finite Difference Formulation on Surface 1 [1]

The net conductive heat flow can be found as

$$Q_{cond} = \frac{kt\Delta z}{\Delta x}(T_{m+1,n} + T_{m-1,n} - 2T_{m,n}) + \frac{kt\Delta x}{\Delta z}(T_{m,n+1} + T_{m,n-1} - 2T_{m,n}) \quad (18) \quad [1]$$

where  $\Delta x$  and  $\Delta z$  are the distances between nodes in the  $x$  and  $y$  directions respectively.

$m$  and  $n$  are the node numbers of the adjacent nodes as seen in Figure 5.

#### 2.1.4.3. Radiation

The net radiative heat transfer from element  $j$  to element  $k$  is defined as

$$Q_{rad,j-k} = \frac{\sigma(T_k^4 - T_j^4)}{\frac{1 - \varepsilon_j}{\varepsilon_j A_j} + \frac{1}{A_j F_{j-k}} + \frac{1 - \varepsilon_k}{\varepsilon_k A_k}} \quad (19) \quad [1]$$

where  $\sigma$  is the Stefan–Boltzmann constant,  $\varepsilon$  is the surface emissivity,  $T$  is the absolute temperature,  $A$  is the surface area, and  $F_{j-k}$  is the radiation view factor between the

elements. In Eq (19) both elements are assumed to be diffuse, gray, and isothermal. The total radiative heat flow from element  $j$  to the rest of the model is

$$q_{rad,j} = \sum_{k=1}^N q_{rad,j-k} \quad (20)$$

where  $N$  is the total number of elements in the model.

#### 2.1.4.4. View Factor

The radiation view factor, also known as the exchange factor, is the percentage of radiation leaving surface  $A_1$  that is incident upon surface  $A_2$ , as shown in Figure 6.

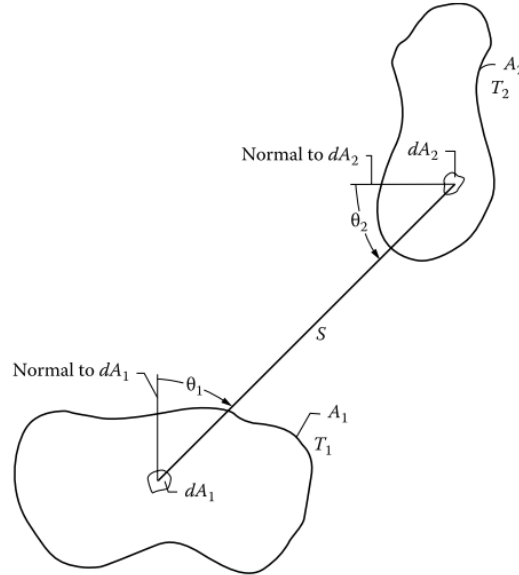


Figure 6: View Factor Between Two Finite Areas [23]

$$F_{A_1-A_2} = \frac{1}{A_1} \int_{A_1} \int_{A_2} \frac{\cos(\theta_1)\cos(\theta_2)}{\pi S^2} dA_1 dA_2 \quad (21) \quad [23]$$

where  $S$  is the vector between differential areas  $dA_1$  and  $dA_2$  on surfaces  $A_1$  and  $A_2$ , and  $\theta_1$  and  $\theta_2$  are the angles between  $S$  and the normal vectors for surfaces  $A_1$  and  $A_2$  respectively. The view factor is integrated across the surfaces  $A_1$  and  $A_2$ .

It is important to note that the sum of the view factors from surface 1 to every other surface and to space must be equal to unity. Therefore, the view factor to space can be found simply as

$$F_{1-space} = 1 - \sum_{n=2}^4 F_{1-n} \quad (22)$$

for surface number  $n$ .

#### 2.1.4.5. *Effective Emissivity*

Recall from section 1.1 that the effective emissivity of a cavity is defined as the ratio of the radiative emission from the cavity opening with the emission from a blackbody with the same base area and reference temperature. In this problem we take the reference temperature to be that of surface 4. A blackbody surface emits the maximum amount of heat for a given temperature and is an ideal surface that serves as a reference to measure the efficiency of all other emitting surfaces. Of key importance is that this reference blackbody is not in a cavity, but rather a flat plate with a clear view to space.

$$\varepsilon_{eff} = \frac{Q_{cavity-space}}{Q_{blackbody-space}} = \frac{\sum_{n=1}^4 Q_{n-space}}{A_4 \sigma (T_4^4 - T_{space}^4)} \quad (23)$$

where  $Q_{n-space}$  is the heat rejected to space from surface  $n$  and  $A_4$  is the area of surface 4.

Since the cavity is nonisothermal, it is not obvious where the reference temperature should be measured for the  $\varepsilon_{eff}$  calculation. In fact, the  $\varepsilon_{eff}$  could be greater than unity if the reference temperature is measured from the “incorrect” location, such as the lip of the cavity wall [24]. The reference temperature is therefore measured at surface 4 both because this is the most important temperature from an engineering perspective, and to ensure that  $\varepsilon_{eff}$  does not exceed unity.

## 2.2. Thermal Desktop

### 2.2.1. Background

Thermal Desktop® is a software package produced by Cullimore & Ring Technologies® (“C&R Tech”) which is specifically designed for use in the thermal aerospace industry. It is built as an application within AutoCAD®, which is produced by Autodesk® [25].

Thermal model objects within Thermal Desktop may be finite difference surfaces, finite difference solids, or finite element solids. Surfaces are 2D objects and represent geometries in which there is no temperature gradient through the thickness of the material. Solids are 3D objects implementing either the finite difference or finite element methods. In Thermal Desktop, finite difference is more robust and more commonly used. In this thesis 2D finite difference surfaces are used to construct the isogrid array.

Any thermal object may be defined with boundary nodes, which are set at a user prescribed temperature. The boundary node implies an infinitely large thermal mass, and thus remains at a constant temperature throughout the calculations. In this thesis boundary nodes are used to construct surface 4 and maintain it at the prescribed temperature.

Radiative heat transfer is the area in which Thermal Desktop differs from other modelling software. While radiative couplings may be defined explicitly between objects, it is highly recommended to utilize Thermal Desktop’s built-in Monte-Carlo ray-racing routines in the RadCAD® module. RadCAD utilizes Monte-Carlo ray-racing to calculate the radiation view factors between every node in the model within a defined radiation analysis group. RadCAD is discussed further in section 2.2.2.

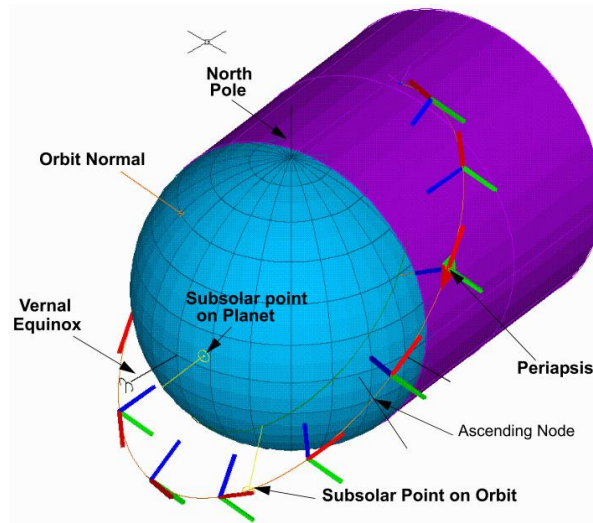


Figure 7: Orbit in Thermal Desktop [25]

One of the unique features in Thermal Desktop is its ability to easily implement environmental heat loads in an orbit. Along with full customization of the orbital parameters, the user may input the solar flux, planetary IR flux, planetary albedo, and other parameters for any celestial body of interest. These parameters play a large role in the overall thermal environment in which the spacecraft is located. The spacecraft may also be set to change its attitude in various points in the orbit as well as vary in time. In addition, a subset of the spacecraft can be set to move independently throughout the orbit and throughout time, for example a gimballed solar array tracking the sun. Environmental heat loads are not considered in the isogrid model presented in this thesis.

## 2.2.2. RadCAD

### 2.2.2.1. Introduction

RadCAD® is a Thermal Desktop module used to calculate environmental heating rates (from The Sun, Earth, etc.) and radiation exchange factors between components

within the thermal model [25]. RadCAD utilizes the Monte-Carlo ray-racing method for radiation exchange factor determination. In this scheme, a finite number of rays (each of which can be thought of as a photon with a finite energy based on the emitting surface's properties and temperature) are emitted from each node in the model. When the ray hits another surface, a portion of its energy is either absorbed, transmitted, or reflected based on the optical properties of the receiving surface. The ray continues to propagate throughout the model either until its energy is reduced below some threshold set by the user (at which point it is considered to be fully absorbed) or is emitted to space. Tracing several thousand rays from each node in the model gives very accurate exchange factors between the model's surfaces [25]. These exchange factors are equivalent to the view factors discussed in section 2.1.4.4.

2.2.2.2. *View Factor RadCAD Solutions vs Textbook Solutions*

In order to validate RadCAD we shall compare the view factors found from a textbook and those calculated by RadCAD for three different geometries. A comparison of the results for each geometry can be found below in Table 1.

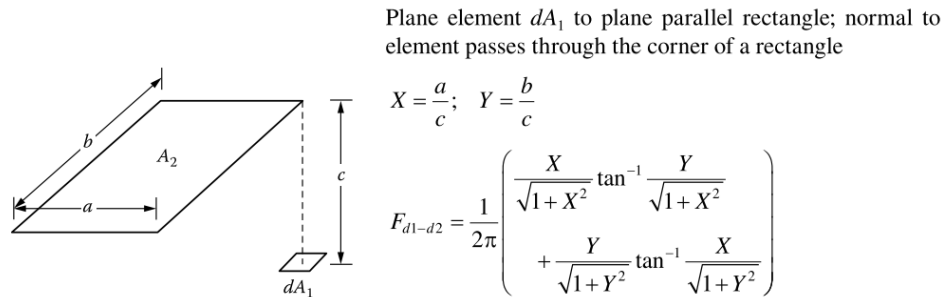


Figure 8: Geometry 1 View Factor [23]

For the above geometry we compute the view factor relation taking  $a = 30\text{cm}$ ,  $b = 50\text{cm}$ , and  $c = 60\text{cm}$ . Note that in this example  $dA_1$  is a differential area.

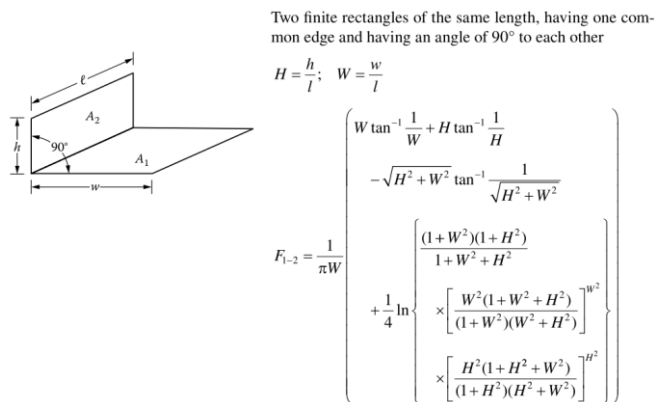


Figure 9: Geometry 2 View Factor [23]

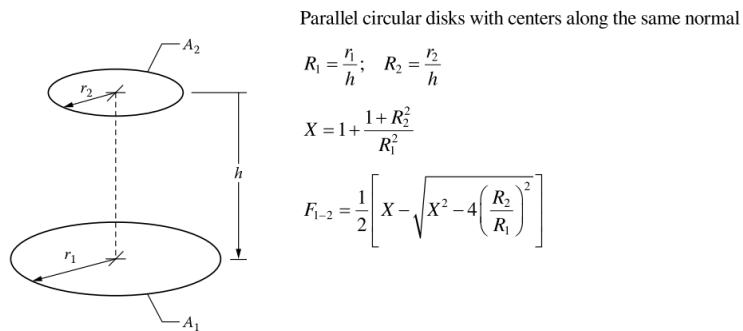


Figure 10: Geometry 3 View Factor [23]

Table 1: Textbook vs RadCAD View Factor Comparison Results

Geometry	Textbook	RadCAD	Absolute Error
1	0.083	0.085	2.0E-03
2	0.111	0.111	3.5E-04
3	0.033	0.033	2.4E-04

Geometries 2 and 3 give identical results between the textbook solution and RadCAD. Geometry 1 has a much larger error than that of the others. This is due to the fact that the textbook solution is for a differential area  $dA_1$ , while Thermal Desktop

requires finite surfaces in order to calculate the exchange factors. RadCAD can calculate the view factors to an arbitrary level of precision if given enough rays to shoot from each node.

### 2.2.3. SINDA

#### 2.2.3.1. *Introduction*

The Systems Improved Numerical Differencing Analyzer (SINDA) is a robust finite difference solver specifically designed for use in thermal applications. SINDA has been a mainstay in an array of industries for over fifty years [26]. It uses the resistor-capacitor (R-C) network representation of thermal systems on which to apply the finite-difference method. The R-C representation is a lumped-capacity method whereby the thermal mass of a portion of the geometry is lumped into a discrete infinitesimal point (a node). Each node has an associated area or volume (depending on the type of thermal object) from which its properties are determined. Each node acts as a capacitor in the electrical analogy, storing and releasing thermal energy based on its thermal capacitance and mass [26].

Nodes exchange energy via resistors which can represent conduction, convection, or radiation. The conduction between nodes within the same surface or solid is determined by the thermal conductivity, cross sectional area, and distance between the nodes. Radiative resistors are found using the areas, emissivities, and view factor between two interacting nodes [26].

2.2.3.2. *Example 1: 1D Steady State Conduction with Heat Generation*

In order to validate Thermal Desktop and SINDA let us model several textbook example problems. The first problem shown below concerns one dimensional steady state conduction with heat generation from the textbook [1]. The problem statement and diagram are shown in Figure 11. A Thermal Desktop model of the example problem is shown in Figure 12.

**EXAMPLE 3.7**

A plane wall is a composite of two materials, A and B. The wall of material A has uniform heat generation  $\dot{q} = 1.5 \times 10^6 \text{ W/m}^3$ ,  $k_A = 75 \text{ W/m} \cdot \text{K}$ , and thickness  $L_A = 50 \text{ mm}$ . The wall material B has no generation with  $k_B = 150 \text{ W/m} \cdot \text{K}$  and thickness  $L_B = 20 \text{ mm}$ . The inner surface of material A is well insulated, while the outer surface of material B is cooled by a water stream with  $T_\infty = 30^\circ\text{C}$  and  $h = 1000 \text{ W/m}^2 \cdot \text{K}$ .

1. Sketch the temperature distribution that exists in the composite under steady-state conditions.
2. Determine the temperature  $T_0$  of the insulated surface and the temperature  $T_2$  of the cooled surface.

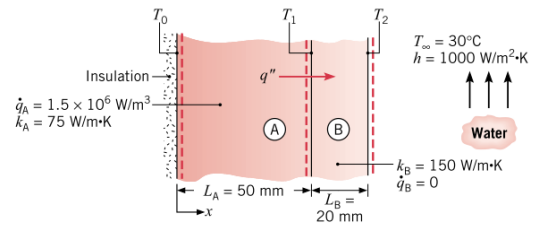


Figure 11: Example Problem 1 Description [1]

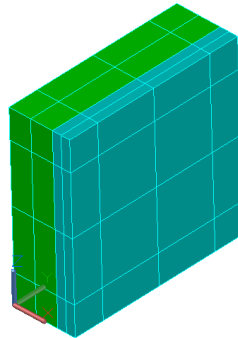


Figure 12: Example Problem 1 Thermal Desktop Model

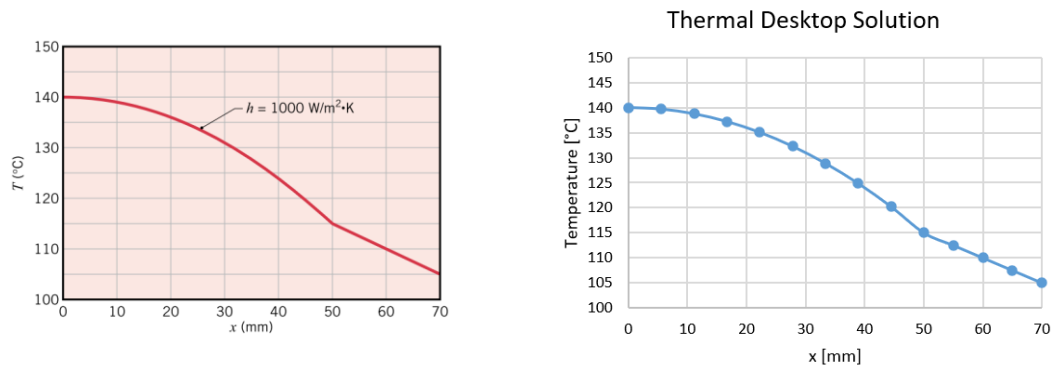


Figure 13: Example Problem 1 Solution [1]

As seen above in Figure 13, the analytical solution and the Thermal Desktop solution exactly match, as expected. It is important to note that due to the finite difference method the Thermal Desktop temperature profile in section A of the wall ( $0 \leq x \leq 50$ ) varies linearly between each node, as opposed to a smooth second order variation in the analytical solution. Despite this, the temperatures at the interfaces between sections A and B, and between B and the fluid are identical to those of the analytical solution.

### 2.2.3.3. Example 2: 3D Transient Conduction

Let us now validate Thermal Desktop for a three-dimensional transient heat conduction problem. Figure 14 below shows the example problem to be solved, again from the textbook [1].

**EXAMPLE 5S.1**

In a manufacturing process stainless steel cylinders (AISI 304) initially at 600 K are quenched by submersion in an oil bath maintained at 300 K with  $h = 500 \text{ W/m}^2 \cdot \text{K}$ . Each cylinder is of length  $2L = 60 \text{ mm}$  and diameter  $D = 80 \text{ mm}$ . Consider a time 3 min into the cooling process and determine temperatures at the center of the cylinder, at the center of a circular face, and at the midheight of the side. Note that Problem 5.124 requires a numerical solution of the same problem using *FEHT*.

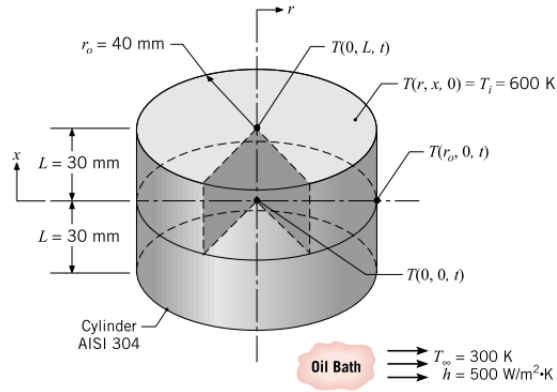


Figure 14: Example Problem 2 Description [1]

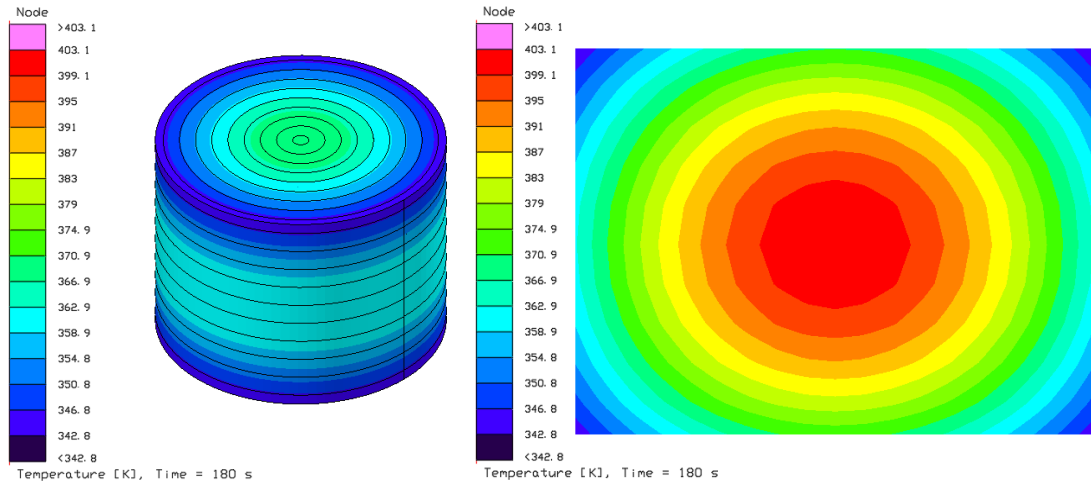


Figure 15: Example Problem 2 Thermal Desktop Temperature Profile

Figure 15 above shows the temperature profile of the cylinder calculated by Thermal Desktop after submersion in the oil bath for 180 seconds.

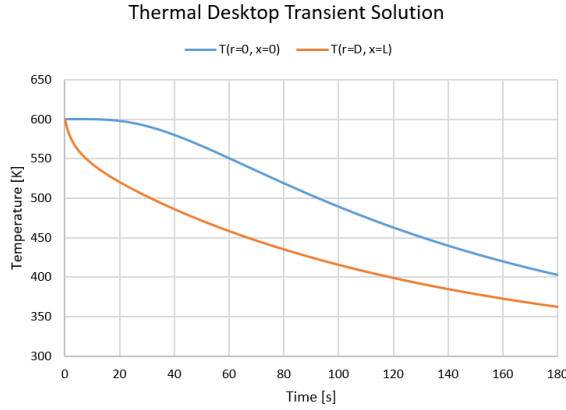


Table 2: Analytical vs Thermal Desktop Results

	Analytical Solution	Thermal Desktop	Absolute Error
$T(0, 0, 3 \text{ min})$	405.0	403.1	1.9
$T(r_0, L, 3 \text{ min})$	365.0	362.4	2.6

Figure 16: Example Problem 2 Thermal Desktop Solution

Figure 16 shows the transient solution for two points on the cylinder. As expected, the point on the outer edge,  $T(D, L)$ , quickly cools down from its initial temperature, while the point in the center of the cylinder,  $T(0, 0)$ , does not greatly change temperature until approximately 20 seconds after submersion. Table 2 shows a comparison between the textbook analytical solution and that of Thermal Desktop. The results are very close and may be improved to an arbitrarily small error by applying a smaller timestep within Thermal Desktop.

### 2.3. Thermal Desktop Final Mathematical Formulation

As discussed in section 2.2.3.1, Thermal Desktop and SINDA use the resistor-capacitor (R-C) network representation of thermal systems on which to apply the finite-difference method. Each node acts as a capacitor in the electrical analogy, storing and releasing thermal energy based on its thermal capacitance and mass. Nodes are connected to each other with conduction, radiation, and/or convection paths depending on the model geometry. The paths between nodes are sometimes referred to as “conductors” with values given as the thermal conductance, which is simply the inverse of the thermal resistance.

The term “conductor” is a slight misnomer as there can exist multiple conduction, convection, and radiation heat transfer “conductor” paths acting in parallel from a single node [26].

Thermal Desktop utilizes the finite difference method for conduction between nodes, the formulation of which was discussed in section 2.1.4.2. Radiation view factors are calculated using the RadCAD module which implements Monte Carlo ray tracing, as discussed in section 2.2.2. This is done to numerically solve the general 3D heat diffusion equation, Eqn (15), with radiative boundary conditions. The radiative heat flux is not explicitly defined, but rather calculated via Monte Carlo ray tracing.

Assuming there is no convection, the final steady state energy balance equation on node  $i$  is

$$Q_i = \sum_{i=1}^M Q_{cond,i-j} + \sum_{i=1}^N Q_{rad,i-j} = 0 \quad (24)$$

Where  $M$  is the number of nodes conductively coupled to node  $i$ , and  $N$  is the total number of nodes in the model. The conduction from node  $i$  to node  $j$  is

$$Q_{cond,i-j} = \frac{kA_{i-j}}{L_{i-j}}(T_j - T_i) \quad (25)$$

where  $k$  is the thermal conductivity,  $A_{i-j}$  is the cross-sectional area between the nodes,  $L_{i-j}$  is the distance between the nodes, and overall  $\frac{kA_{i-j}}{L_{i-j}}$  term is the thermal conductance.

The radiation exchange from node  $i$  to node  $j$  shown below is a slightly modified version of Eqn (19)

$$Q_{rad,i-j} = \frac{\sigma(T_j^4 - T_i^4)}{\frac{1 - \varepsilon_i}{\varepsilon_i A_i} + \frac{1}{A_i F_{i-j}} + \frac{1 - \varepsilon_j}{\varepsilon_j A_j}} \quad (19) \quad [1]$$

where the view factor  $F_{i-j}$  is calculated via Monte-Carlo ray tracing as described in section 2.2.2.

Equation (24) is developed for every node in the model. The system of equations for all nodes are collected into a single matrix and solved for simultaneously using an iterative advanced algebraic multigrid solver which exploits the conjugate gradient method, called AMG-CG [26].

## **2.4. Thermal Desktop Isogrid Model**

A Thermal Desktop thermal model of an isogrid cavity array was developed. The array is constructed of 2D finite difference surfaces for the cavity walls and base. The thickness of the cavity walls is only used in the finite difference conduction formulation as described in section 2.1.4.2. Even if the walls are given an arbitrarily large thickness, the physical geometry of the wall remains 2D. This means that the view factor calculations from each surface are independent of the wall thickness. Modelling the surfaces as 2D objects preserves the assumption that the wall is isothermal through its thickness.

Recall from section 2.1.3 that the base of the isogrid array is assumed to be at a prescribed base temperature,  $T_b$ . In the model we set  $T_b = 300K$ . This prescribed base temperature and the fact that the isogrid array is in space are the only boundary conditions present. There is no prescribed heat flux on the cavity. The radiative heat flux is implicitly calculated by Thermal Desktop as described in section 2.3.

### **2.4.1. Determining Appropriate Isogrid Array Size**

Unlike various other modelling software Thermal Desktop does not have the ability to impose a cyclic boundary condition, which could be used to approximate an infinite

array. This presents an issue as one of the assumptions made in section 2.1.2 is that of a single cell immersed within an arbitrarily large array of isogrid. The question then becomes: what is the minimum array size necessary to approximate an infinitely large isogrid array? To answer this question, several Thermal Desktop models were made of rectangular isogrid arrays of various sizes, as shown below in Figure 17.

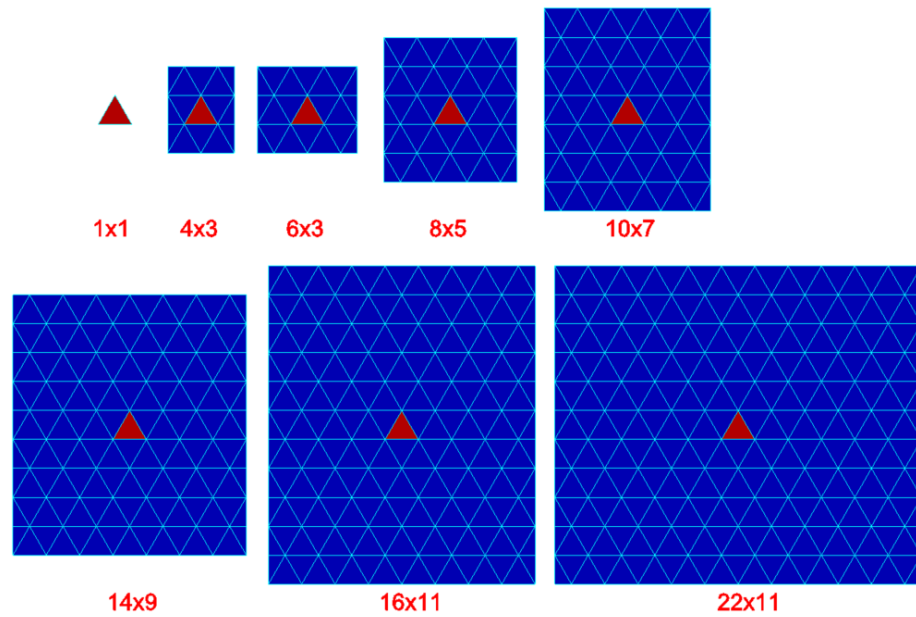


Figure 17: Varying Rectangular Isogrid Array Size

This model was tested with a cavity parameters  $L = 200mm$ ,  $H = 100mm$ ,  $t = 2mm$ , and  $\epsilon_{surf} = 0.70$ . The results of varying the array size on the  $\epsilon_{eff}$  of the center cell are shown in Figure 18.

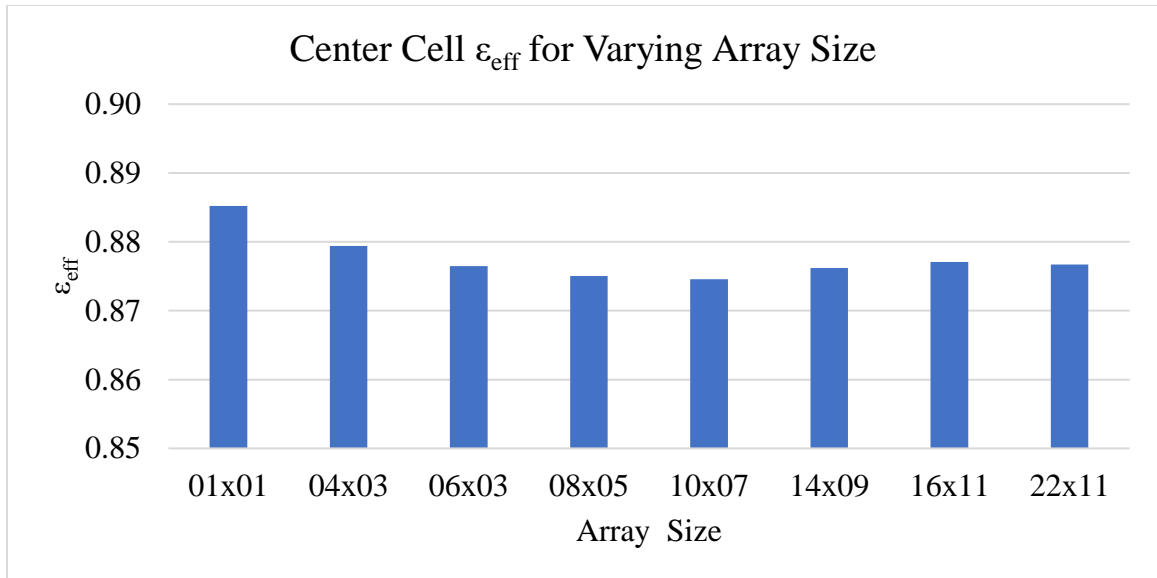


Figure 18: Center Cell  $\epsilon_{eff}$  for Varying Array Size

The array size does play a role in the center cell's  $\epsilon_{eff}$ , but after the addition of a few cells the effect is diminished. Edge effects are discussed further in section 3.7.

#### 2.4.2. Isogrid Model Overview

Based on these results from section 2.4.1 it was decided to create a rectangular isogrid array of 22x11 cells with the cavity of interest located directly in the center. This arrangement gives the central cavity 10.5 cells to the edge in the  $x$  direction, and 5 cells in the  $y$  direction. In Figure 19 below the central cavity is shown in red.

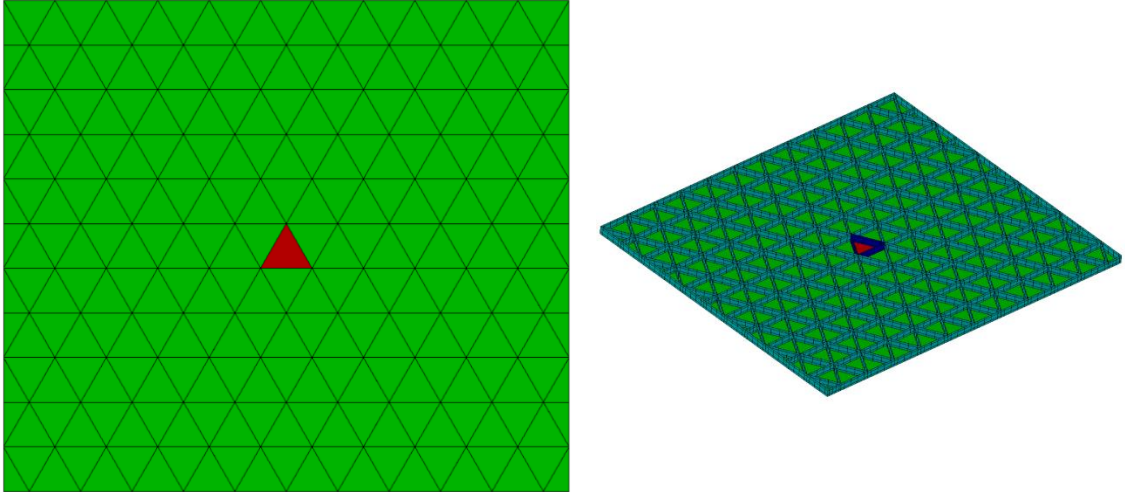


Figure 19: Thermal Desktop Isogrid Array Model

In the model the only radiative exchange with space takes place in the  $+z$  direction, through the cavity opening. There is no radiative heat transfer to space either from the outer surface of the model, nor from the back of the array in the  $-z$  direction.

#### 2.4.3. Effect of the Wall Nodalization on $\epsilon_{eff}$

In order to determine the appropriate level of nodalization on the cavity walls, a mesh coarseness sensitivity study was conducted. Section 3.4.4 will show the importance of accurate knowledge of the temperature gradient in determining the overall  $\epsilon_{eff}$  at any given  $\eta$  for a nonisothermal cavity. Due to the finite difference method, the only way to accurately capture this nonlinear temperature profile is by discretizing the wall into more elements (nodes). The effect of varying the nodalization (also referred to as the mesh coarseness or discretization) is shown below in Figure 20, where  $\eta$  is the nondimensional wall height and  $\lambda$  is the nondimensional wall thickness, both of which are defined in section 3.1.

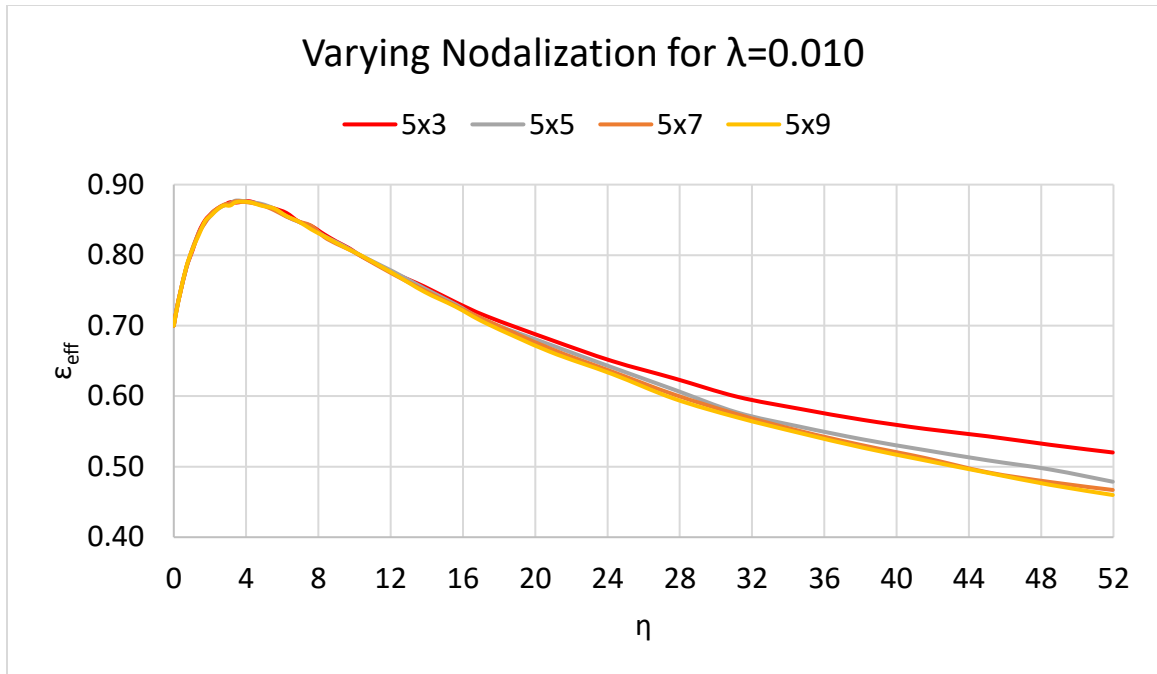


Figure 20: Varying Nodalization for  $\eta = 0.010$

There is good agreement between the nodalizations for small values of  $\eta$ , due to the small temperature gradient. The differences between the nodalizations only becomes significant for larger  $\eta$ , in this case approximately  $\eta > 20$ . As a majority of the Thermal Desktop model runs were completed with a 5x3 nodalization, the results for this chapter are only presented for the range  $0 \leq \eta \leq 20$ . This  $\eta$  range was determined to be acceptable because all cases analyzed have their  $\eta_{crit} < 20$ , which is the most important value to have knowledge of from an engineering perspective.

## Chapter 3: Results

### 3.1. Model Parameters

#### 3.1.1. Nondimensional Wall Height ( $\eta$ )

Recall the coordinate system from section 2.1.1. Figure 4 is reproduced below for convenience.

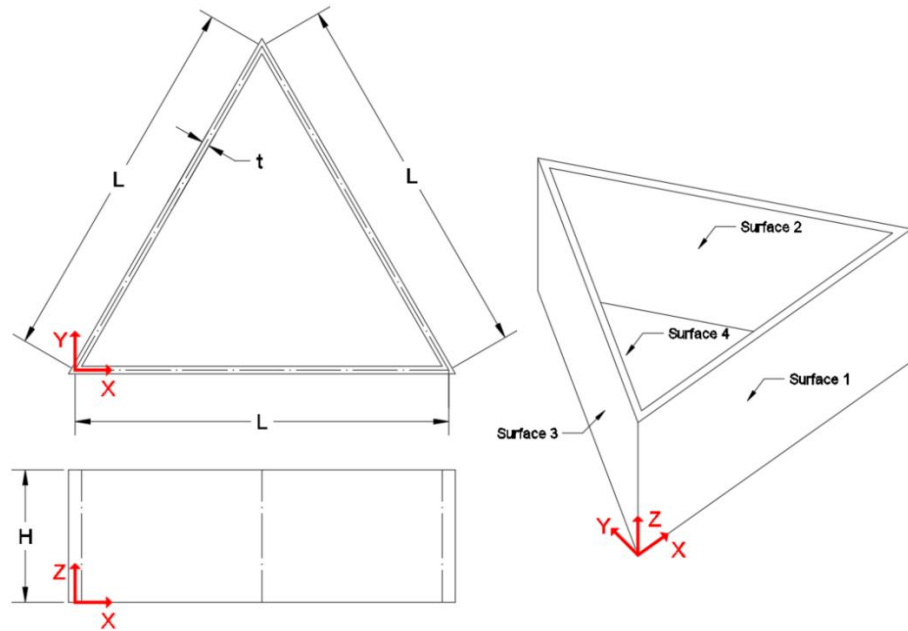


Figure 4: Coordinate System for the Isogrid and Designation of Its surfaces

The main nondimensional parameter used in this work is  $\eta$ , which is defined as the ratio of a cavity's inner wall surface area with that of its base. For the case of isogrid

$$\eta = \frac{A_{walls}}{A_{base}} = \frac{3LH}{L^2\sqrt{3}/4} = \frac{12H}{\sqrt{3}L} \quad (26)$$

where  $L$  and  $H$  are the isogrid's length and height respectively and are shown above in Figure 4. The reason for using  $\eta$  instead of various other nondimensional parameters is that the relationship between  $\eta$  and  $\varepsilon_{eff}$  holds for cavity geometries beyond just isogrid. This

is discussed further in section 3.8. An  $\eta$  value of 3.46 is used throughout this chapter because it represents the height at which  $H = L/2$ .

In the model,  $L = 200\text{mm}$  and  $H$  is varied from  $0\text{mm}$  to  $1500\text{mm}$ , resulting in  $\eta$  values within the range of  $0 - 51.96$ . Results are only shown for  $\eta \leq 20$  due to the large temperature gradients and fine nodalization required at these larger  $\eta$  values. This is discussed further in section 2.4.3.

### 3.1.2. Nondimensional Wall Thickness ( $\lambda$ )

The wall thickness is converted to a nondimensional parameter,  $\lambda$ , as the ratio of the wall thickness  $t$  with side length  $L$ .

$$\lambda = t/L \quad (27)$$

In this thesis only very small values of  $\lambda$  are used to maintain the validity of the assumption discussed in section 2.1 that the cavity walls are 2D when calculating the view factors.

In the model,  $t$  ranges from  $0.1\text{mm} - 3\text{mm}$  resulting in a range in  $\lambda$  from  $0.0005 - 0.015$ .

### 3.1.3. Characteristic Wall Resistance ( $R_{char}$ )

The characteristic resistance of the wall is the total resistance in the  $z$  direction.

$$R_{char} = \frac{H}{k(tL)} \quad (28)$$

where  $k$  is the wall material's thermal conductivity, and  $tL$  represents the wall's cross-sectional area in the  $x$ -  $y$  plane. Since  $R_{char}$  is the thermal resistance, it has units of  $^{\circ}\text{C}/W$ .

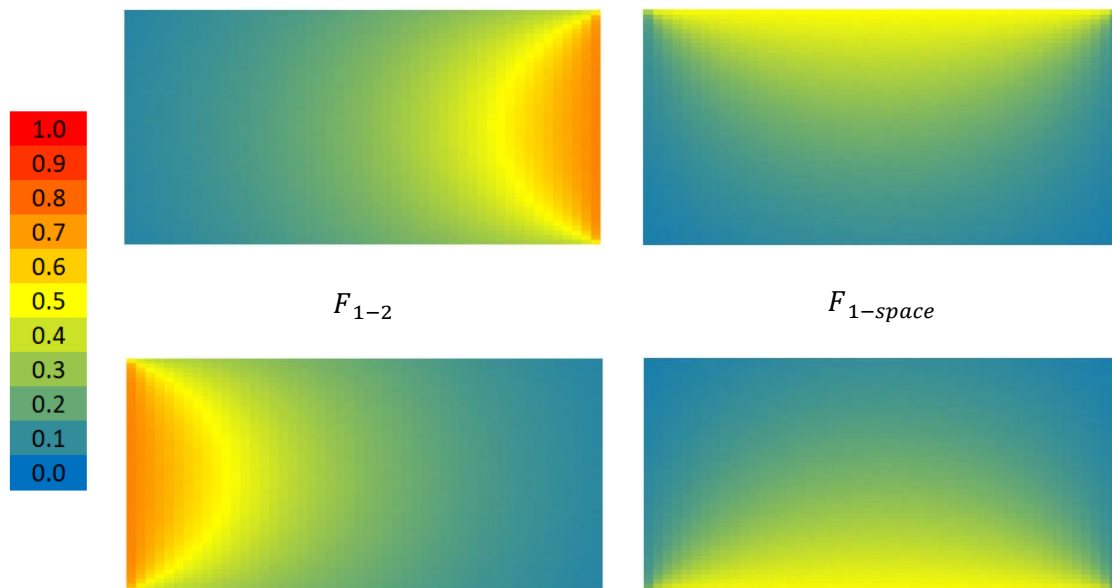
In the model, the isogrid is assumed to be constructed out of aluminum with a thermal conductivity of  $k = 151.5 \frac{W}{mK}$ . This conductivity is held as a constant and is not varied.

### 3.1.4. Base Temperature ( $T_b$ )

The temperature on base of the cavity (surface 4) was held as a constant throughout this study at  $T_b = T_4 = 300K$ . The effect that varying  $T_b$  has on the temperature profile and  $\varepsilon_{eff}$  is left as future work.

## 3.2. View Factors Across Surface 1

Recall from section 2.1.4.4 that the view factor is defined as the percentage of radiation leaving surface leaving surface  $A_1$  that is incident upon some other surface  $A_2$ . Due to the geometry of the isogrid, the view factor varies across each surface and is highly dependent on the  $x$  and  $z$  position. The view factors from surface 1 to surfaces 2, 3, 4, and to space for  $\eta = 3.46$  are shown below in Figure 21.



$$F_{1-3}$$

$$F_{1-4}$$

Figure 21: View Factors Across Surface 1 for  $\eta=3.46$

Due to the geometry's symmetry,  $F_{1-2}$  and  $F_{1-3}$  are mirrored about the line  $X = \frac{L}{2}$ .

Similarly, the view factors  $F_{1-4}$  and  $F_{1-space}$  are mirrored about  $Z = \frac{H}{2}$ .

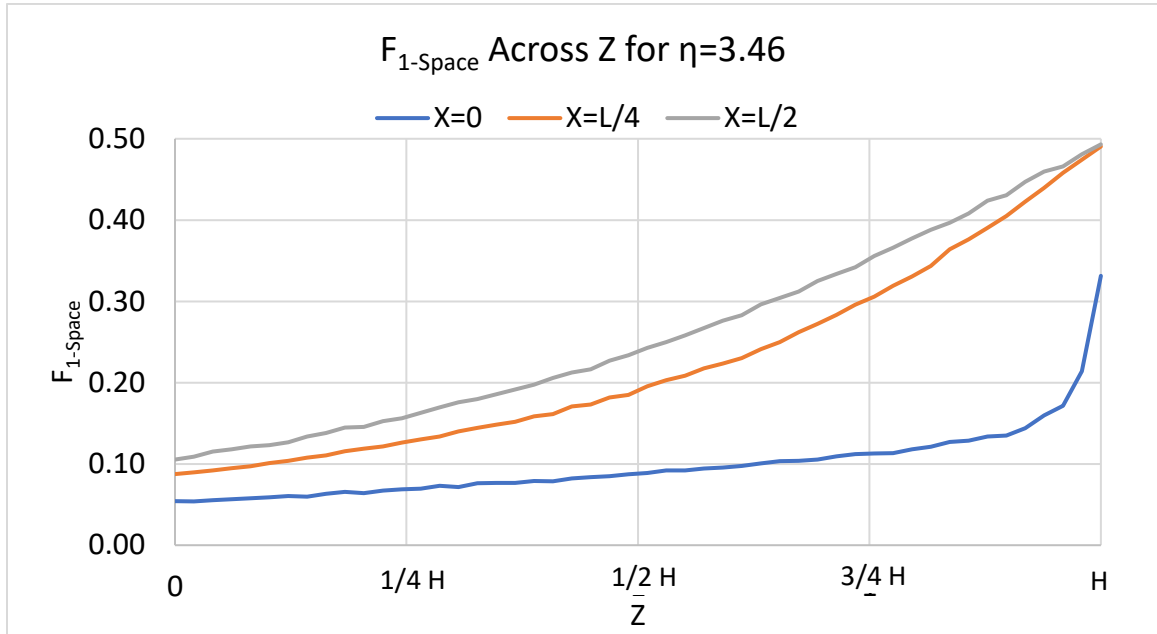


Figure 22:  $F_{1-Space}$  Across  $z$  for  $\eta = 3.46$

Figure 22 above shows the nonlinear nature of  $F_{1-Space}$  as a function of position on the wall in the  $z$  direction. This nonlinearity is especially present in the corners of the cavity at  $x = 0$  and  $x = L$ .

### 3.3. Temperature Profile

The temperature profile across surface 1 is shown in Figure 23, Figure 24, and Figure 25. In these figures the temperatures are reported as deltas with the base temperature ( $T_4 = T_b$ ), such that  $\Delta T(x, z) = T_b - T(x, z)$ .

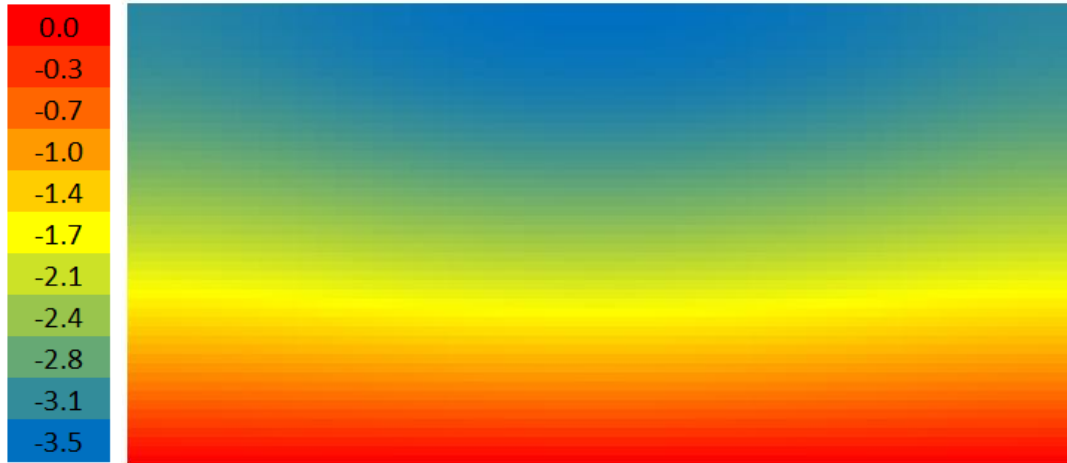


Figure 23:  $\Delta T$  Temperature Profile for  $\epsilon_{surf} = 0.7$ ,  $\eta = 3.46$ ,  $\lambda = 0.010$

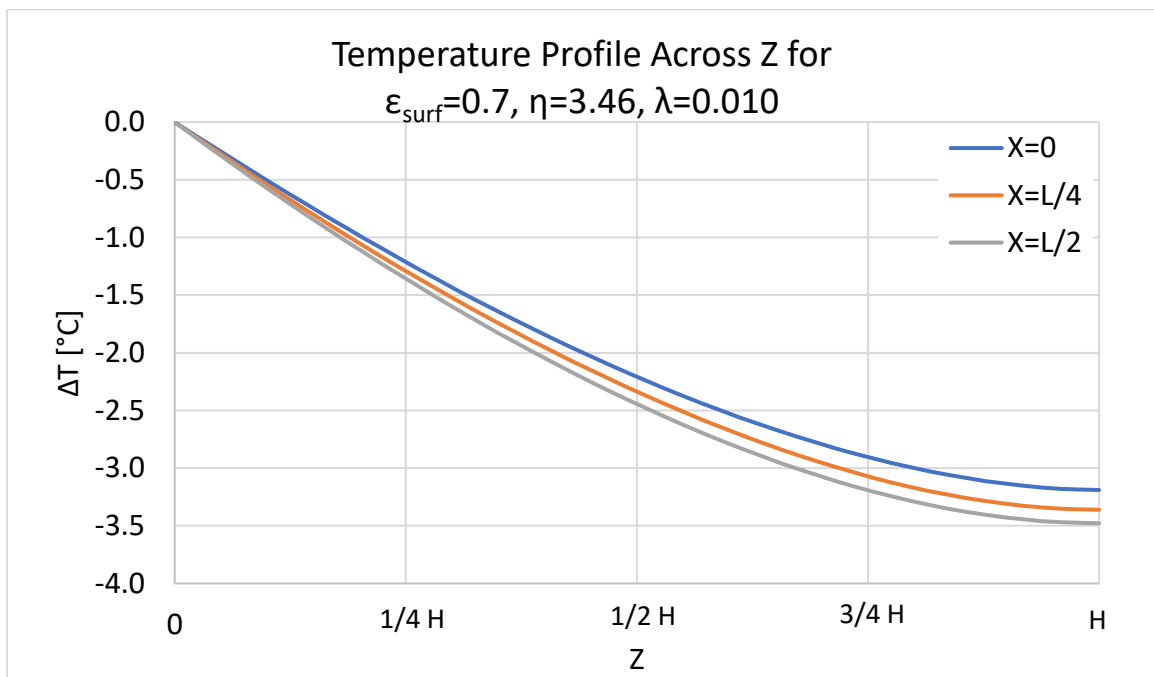


Figure 24:  $\Delta T$  Temperature Profile Across  $z$  for  $\epsilon_{surf} = 0.7$ ,  $\eta = 3.46$ ,  $\lambda = 0.010$

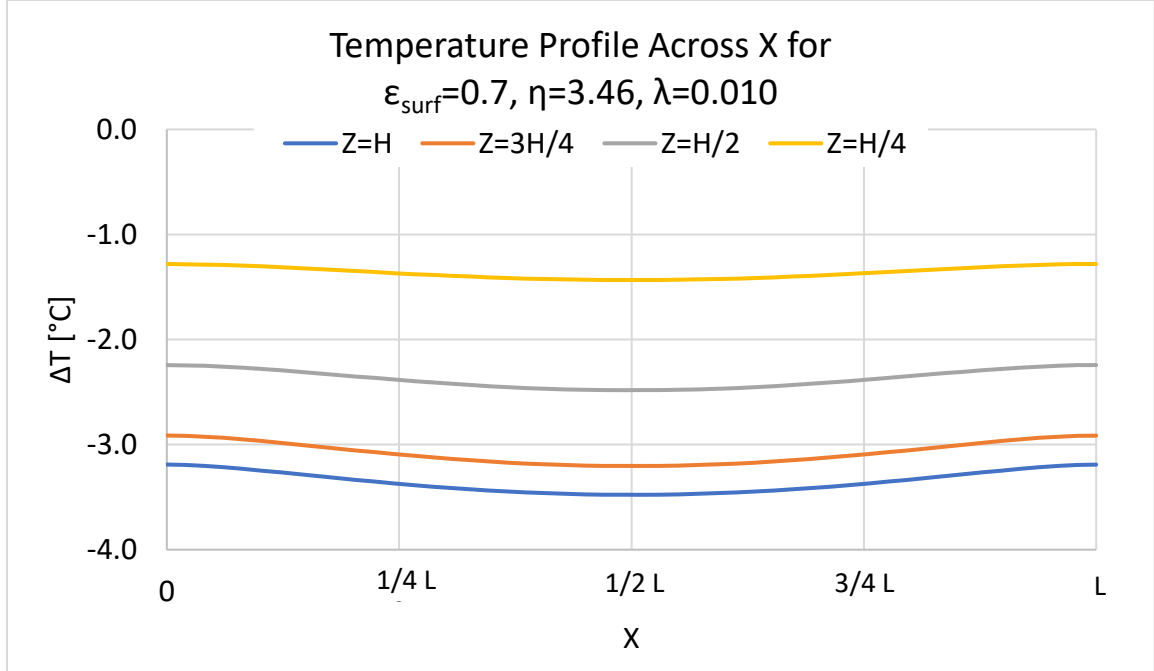


Figure 25:  $\Delta T$  Temperature Profile Across  $x$  for  $\epsilon_{surf} = 0.7$ ,  $\eta = 3.46$ ,  $\lambda = 0.010$

Figure 24 shows that the temperature profile in the  $z$  direction is nonlinear, especially as  $z \rightarrow H$ . Figure 25 shows that the temperature profile across the  $x$  direction is at a minimum at  $x = L/2$  and at maximum at the ends when  $x = 0$  and  $x = L$ . These ends also correspond to an adiabatic condition as discussed in section 2.1.3. The coldest point on surface 1 occurs at  $x = L/2$ ,  $z = H$ . The temperature profile seen in the previous figures is non-linear due to the radiation heat flux on surface 1 to/from the other surfaces and to space. The value of this radiative heat flux is not explicitly defined in the model. Rather it is calculated by Thermal Desktop for each individual node based on the node's temperature, optical properties, and view factors as described in section 2.3.

The maximum  $\Delta T$ , defined as  $T\left(\frac{L}{2}, H\right) - T_b$ , is also a function of  $\eta$  as shown in Figure 26.

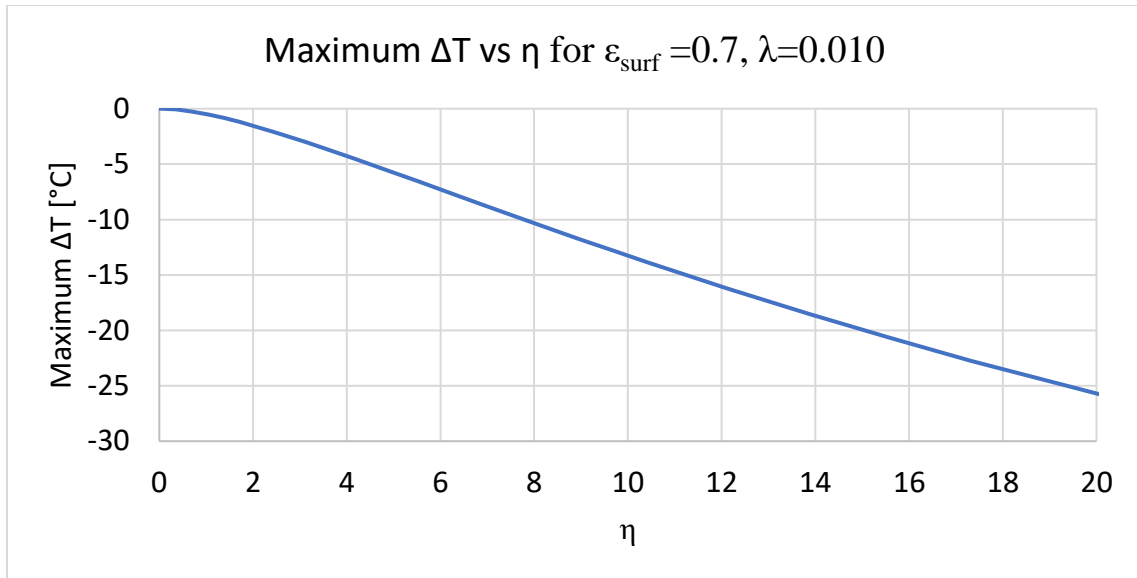


Figure 26: Maximum  $\Delta T$  vs  $\eta$  for  $\epsilon_{surf} = 0.7$ ,  $\lambda = 0.010$

The maximum  $\Delta T$  is inversely proportional to  $\eta$ , due mainly to the fact that the wall's characteristic thermal resistance is a function of  $H$ , and thus directly related to  $\eta$ . The wall's resistance is discussed further in section 3.6.

### 3.4. Effect of Varying Wall Height ( $\eta$ )

#### 3.4.1. Characteristic $\epsilon_{eff}$ vs $\eta$

The characteristic plot of  $\epsilon_{eff}$  vs  $\eta$  is split into three regions, which are qualitatively shown below in Figure 27.

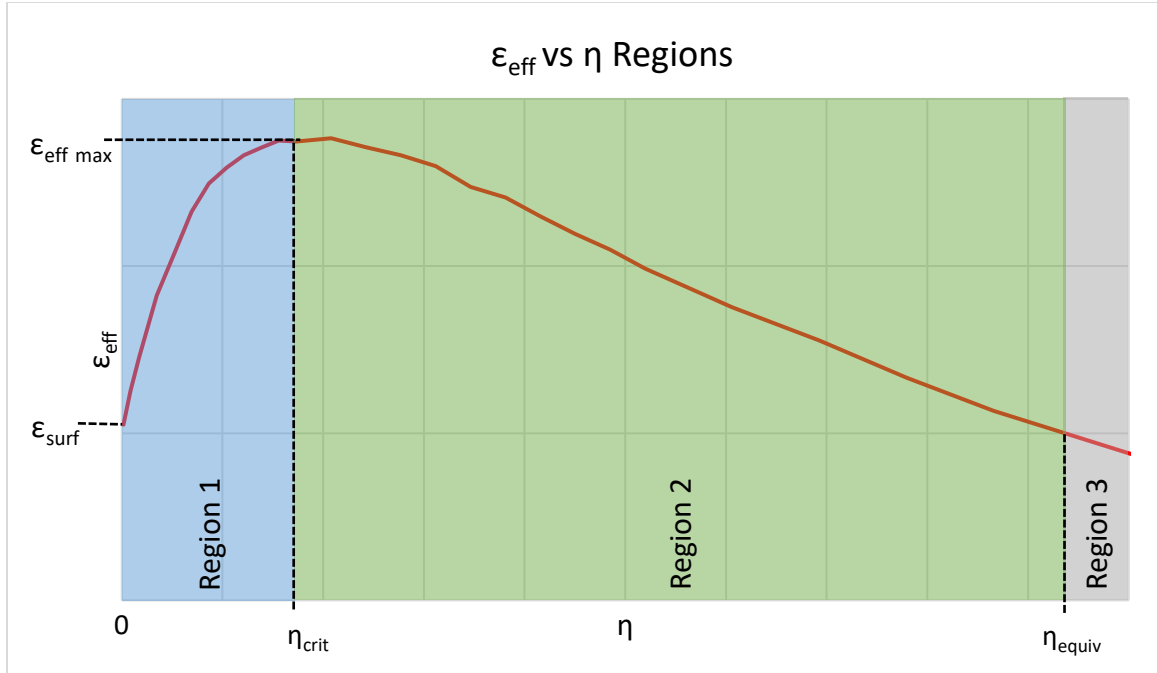


Figure 27: Characteristic Regions of  $\epsilon_{eff}$  vs  $\eta$

As shown in Figure 27,  $\eta_{crit}$  is the critical wall height for which the effective emissivity is at its maximum ( $\epsilon_{eff max}$ ).  $\eta_{equiv}$  is the wall height at which  $\epsilon_{eff} = \epsilon_{surf}$  and is therefore equivalent to that of a flat plate.

The demarcation between regions 1 and 2 is  $\eta_{crit}$ , while the demarcation between regions 2 and 3 is  $\eta_{equiv}$ . Region 1 is characterized by  $\epsilon_{eff}$  monotonically increasing starting at a value of  $\epsilon_{surf}$  at  $\eta = 0$  and ending with a value of  $\epsilon_{eff max}$  at  $\eta_{crit}$ . In region 2,  $\epsilon_{eff}$  monotonically decreases from its maximum value of  $\epsilon_{eff max}$  at  $\eta_{crit}$ , until it reaches  $\epsilon_{surf}$  at  $\eta_{equiv}$ . Region 3 is characterized by  $\epsilon_{eff} < \epsilon_{surf}$  which occurs for  $\eta > \eta_{equiv}$ . It is hypothesized that  $\lim_{\eta \rightarrow \infty} \epsilon_{eff} = 0$ , though this has yet to be tested. Region 1 is the only region in which an isogrid radiator should be designed. This is because in this region  $\epsilon_{eff} > \epsilon_{surf}$  while requiring less total mass than an equivalent  $\epsilon_{eff}$  in region 2.

### 3.4.2. Results of $\epsilon_{eff}$ vs $\eta$

The results of  $\epsilon_{eff}$  vs  $\eta$  for various values of  $\epsilon_{surf}$  are shown in Figure 28. The same data is expanded upon for different values of  $\lambda$  in Table 2.

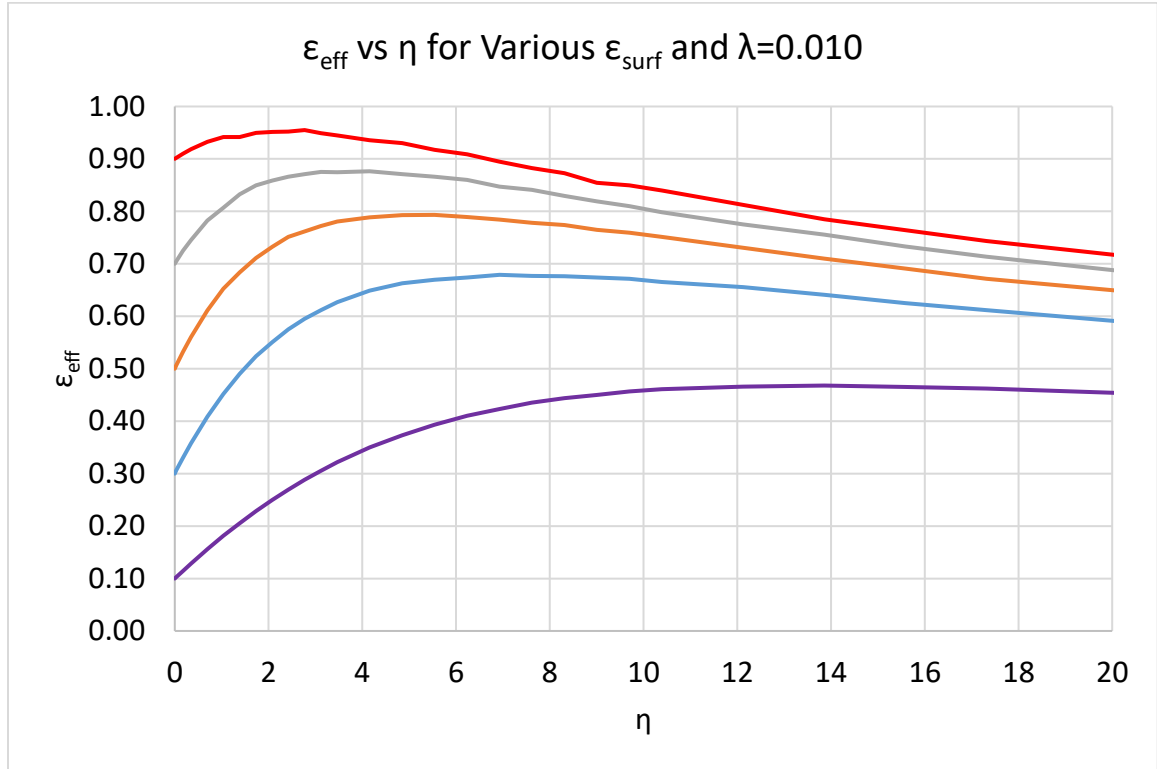


Figure 28:  $\epsilon_{eff}$  vs  $\eta$  for Various  $\epsilon_{surf}$  and  $\lambda = 0.010$

Table 2: Characteristic Regions Tabulated Values

$\lambda$	$\epsilon_{surf}$	$\epsilon_{eff max}$	$\eta_{crit}$	$\eta_{equiv}$
0.005	0.90	0.94	2.08	4.31
	0.70	0.86	2.77	6.31
	0.50	0.77	4.16	>20
	0.30	0.65	5.54	>20
	0.10	0.44	12.12	>20
0.010	0.90	0.95	2.77	6.67
	0.70	0.88	4.16	18.73
	0.50	0.79	5.54	>20
	0.30	0.68	6.93	>20
	0.10	0.47	13.86	>20

0.015	0.90	0.96	2.42	>20
	0.70	0.88	4.16	>20
	0.50	0.81	4.85	>20
	0.30	0.69	8.31	>20
	0.10	0.48	13.86	>20

In Figure 28 and Table 2 it is clear that larger values of  $\epsilon_{surf}$  have correspondingly larger values of  $\eta_{crit}$ ,  $\eta_{equiv}$ , and  $\epsilon_{eff\ max}$ . This makes intuitive sense as one would expect that a cavity with an  $\epsilon_{surf}$  of 0.90 would have a larger  $\epsilon_{eff\ max}$  than that of an identical cavity with an  $\epsilon_{surf}$  of 0.10. However, what is not immediately obvious is that the cavity with the lower  $\epsilon_{surf}$  will have a larger relative increase in the  $\epsilon_{eff\ max}$ . This effect is measured by looking at the ratio  $\epsilon_{eff}/\epsilon_{surf}$ , for various values of  $\epsilon_{surf}$ , below in Figure 29.

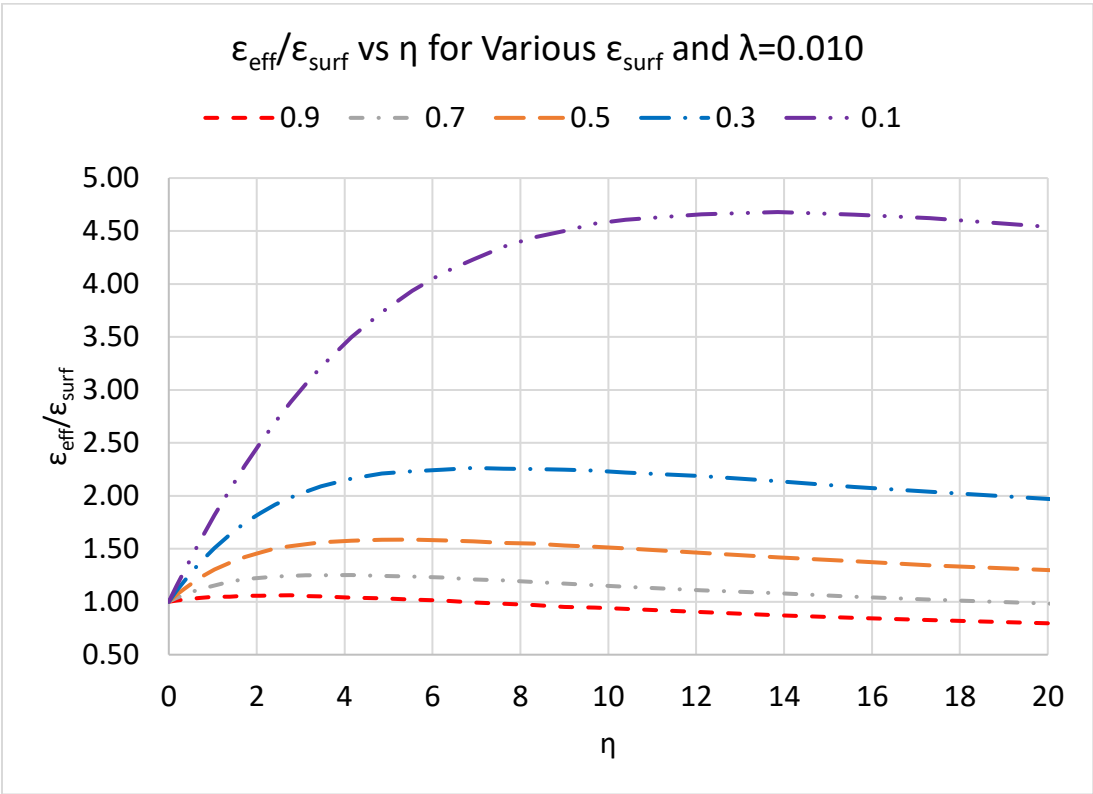


Figure 29:  $\epsilon_{eff}/\epsilon_{surf}$  vs  $\eta$  for Various  $\epsilon_{surf}$  and  $\lambda = 0.010$

As discussed in section 1.1,  $\varepsilon_{eff} \leq 1$  for any case. A cavity with an  $\varepsilon_{surf}$  of 0.90 is already very close to that of a blackbody, and so does not have much “room to grow” by increasing  $\eta$ . On the other hand, a cavity with an  $\varepsilon_{surf}$  of 0.10 has much more room to grow with increased  $\eta$  before it approaches the  $\varepsilon_{eff} \leq 1$  limit. As such, the ratio  $\varepsilon_{eff}/\varepsilon_{surf}$  has a larger maximum value for the lower  $\varepsilon_{surf}$  case, as it both has a smaller value in the denominator and has more room to grow with increased  $\eta$ .

### 3.4.3. Contributions to the Critical Wall Height

The phenomenon of  $\varepsilon_{eff}$  increasing with  $\eta$  until some critical value of  $\eta_{crit}$  is analogous to the classical heat transfer problem of the critical insulation thickness of a pipe. Adding additional layers of insulation decreases the conduction rate from the pipe while simultaneously increases the rate of convection and radiation to the environment due to the increased surface area [1]. There exists a critical insulation thickness beyond which the addition of more insulation causes the overall heat transfer with the environment to increase. In the same way, there exists a critical  $\eta$  for which the  $\varepsilon_{eff}$  is at a maximum (i.e.,  $\eta_{crit}$ ) and beyond which the  $\varepsilon_{eff}$  begins to decrease. The competing factors in this case are the resistance up the cavity walls (in the  $z$  direction), the decreased temperature at the top of the walls (at  $z = H$ ), and the bases’ view factor to space.

The relative effect of the cavity walls (surfaces 1-3) and the base (surface 4) on the overall  $\varepsilon_{eff}$  by can be seen by recognizing that the total effective emissivity can be split into contributions from the base and from the walls:

$$Q_{space} = Q_{base-space} + Q_{walls-space} \quad (29)$$

The effect of these varying factors can be seen in Figure 30 which compares the heat rejected to space from the base and walls of the cavity to that of a reference blackbody.

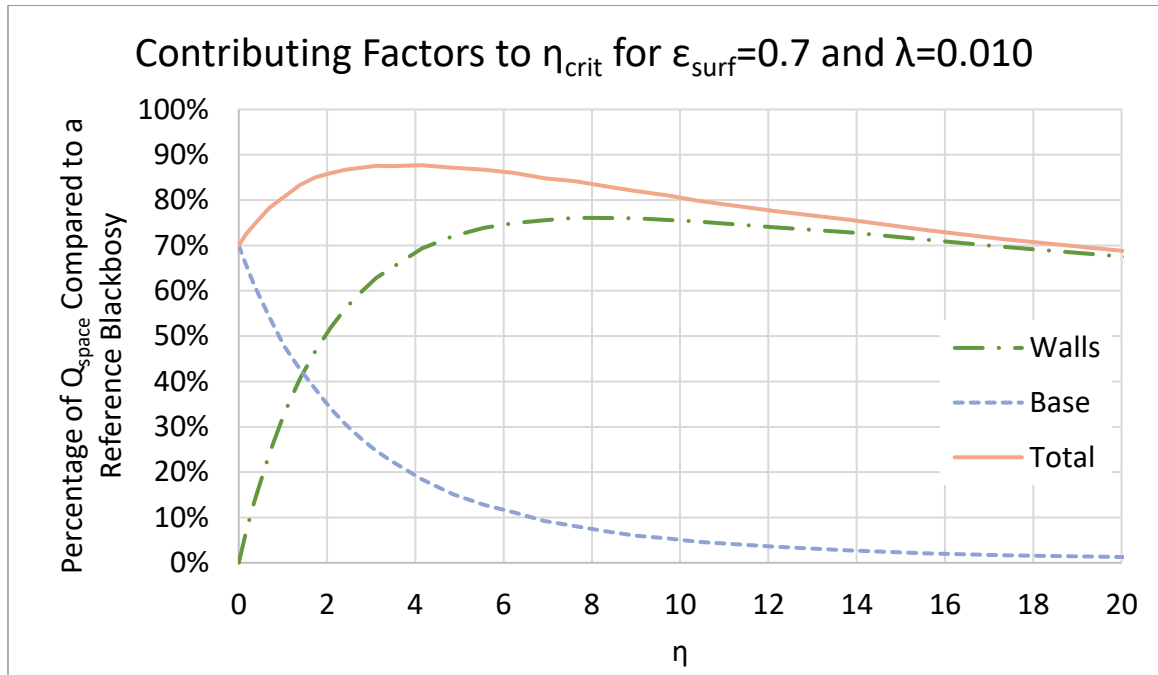


Figure 30: Contributing Factors to  $\eta_{crit}$  for  $\epsilon_{surf} = 0.7$  and  $\lambda = 0.010$

At  $\eta = 0$  the wall height is 0 and  $Q_{walls-space} = 0$  and the entirety of  $Q_{space}$  comes from the cavity base. As  $\eta$  increases, the contribution from the base quickly decreases, as the base's view factor to space is reduced. At the same time, the contribution from the walls increases, the net effect of which is that  $Q_{space}$  also increases while within region 1.

As  $\eta$  increases, the effect of the wall's characteristic resistance becomes more of a factor. The resistance increases linearly with the wall height. This increased resistance makes it more difficult for the walls to wick heat up from the base to the top of the wall where heat may be more efficiently radiated to space. The view factor to space becomes larger towards the top of the wall (as seen in Figure 21), which increases its ability to be rejected to space. Consequently, it is desirable to reduce the resistance associated with the

wall height so that the higher temperature near the top of the wall is coupled with the larger view factor for enhanced radiation heat transfer to space. Due partially to this increased view factor, the temperature of the wall as  $z \rightarrow H$  decreases (as seen in Figure 24). This reduction in temperature significantly decreases the ability for heat to be rejected to space due to the  $T^4$  relationship between temperature and radiative emission (as described in 2.1.4.3). The effect of these factors is that  $Q_{space}$  reaches a maximum value at  $\eta_{crit}$ , and then continues to decrease as  $\eta$  goes beyond  $\eta_{crit}$ .

#### 3.4.4. Isothermal vs Nonisothermal Cavity Walls

Throughout this thesis the assumption has been made that the cavity walls are nonisothermal. If instead the cavity walls are assumed to be isothermal at temperature  $T_b$ , it is found that there is no reduction in  $\varepsilon_{eff}$  after  $\eta_{crit}$ . In this case the  $\varepsilon_{eff}$  approaches some maximum value  $\varepsilon_{eff,max,isothermal}$  as seen in Figure 31. This isothermal condition can be obtained by constructing the cavity out of a material with a very high thermal conductivity.

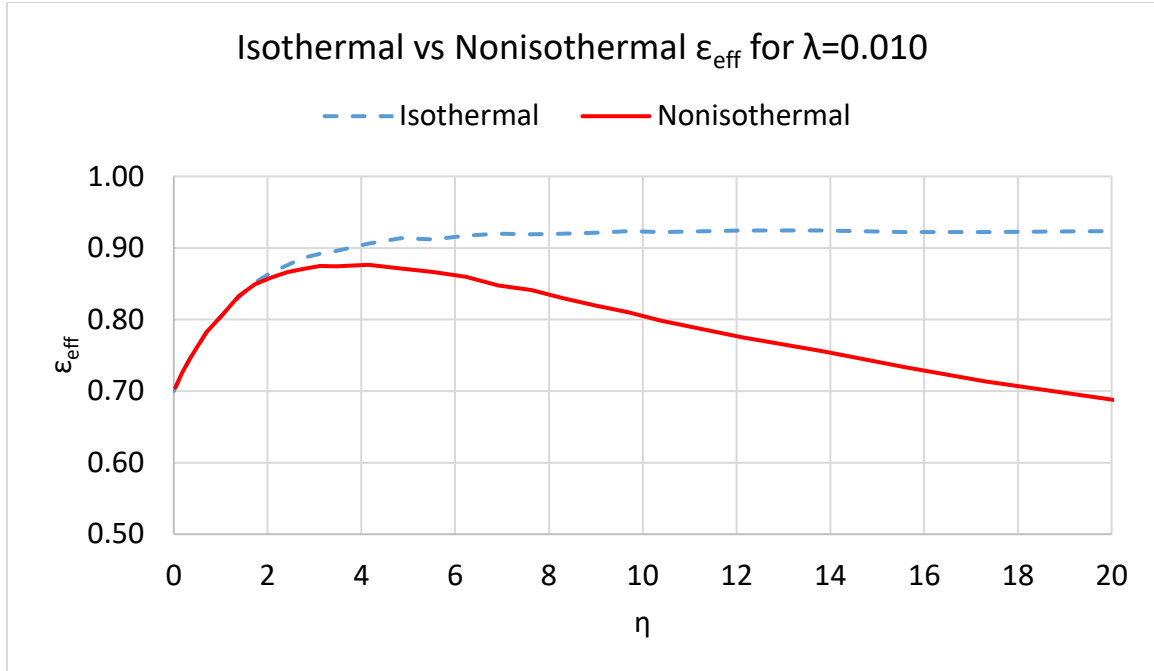


Figure 31: Isothermal vs Nonisothermal  $\epsilon_{eff}$  for  $\lambda = 0.010$

The difference in  $\epsilon_{eff}$  between the isothermal and nonisothermal cases is virtually nonexistent for small values of  $\eta$  (in this case  $\eta < 2$ ). This is due to the small temperature gradient up the walls and the small overall influence of the walls in the  $Q_{space}$  as shown previously in Figure 30. The difference between the isothermal and nonisothermal cases only becomes noticeable with larger values  $\eta$ , and continues to become more significant with ever larger  $\eta$  values. For example, in Figure 31 at  $\eta = 20$  the  $\epsilon_{eff}$  in the isothermal case is 0.92 while in the nonisothermal case it is only 0.68.

### 3.5. Effect of Varying Wall Thickness ( $\lambda$ )

#### 3.5.1. Results of Varying Wall Thickness ( $\lambda$ )

Recall that the nondimensionalized wall thickness,  $\lambda$ , is defined as  $\lambda = \frac{t}{L}$  in section 3. The wall thickness is directly related to the wall resistance (see section 3.1.3)

and thus the amount of heat able to be conducted to the top of the walls. This effect on  $\epsilon_{eff}$  is shown in Figure 32.

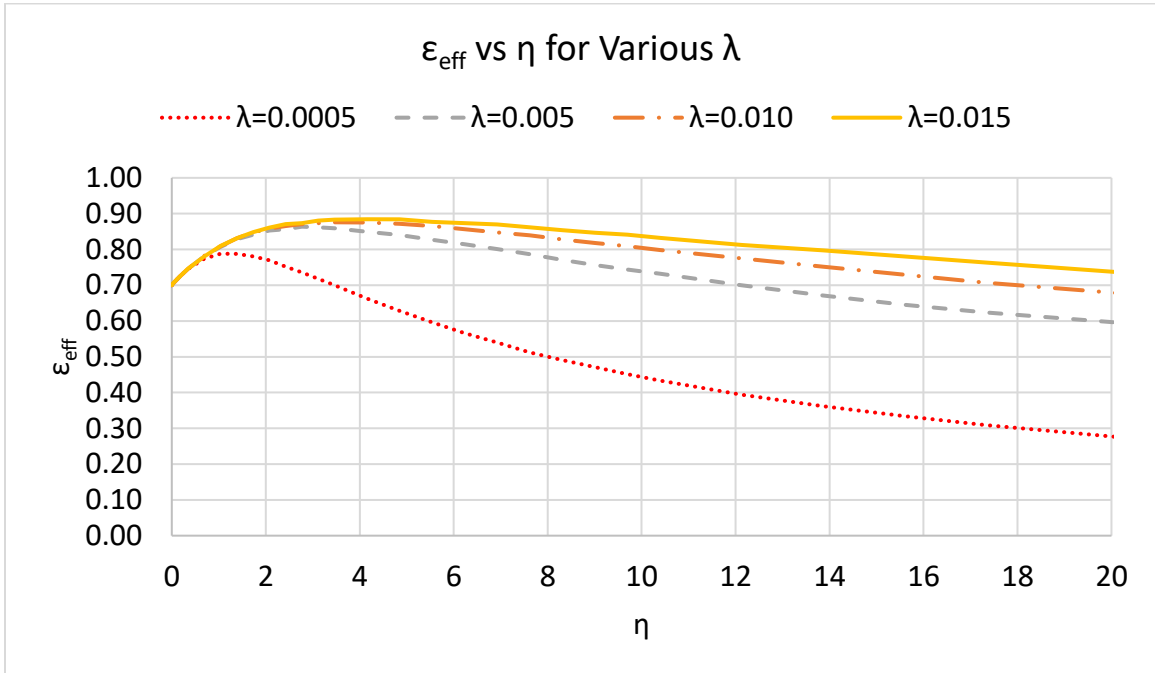


Figure 32:  $\epsilon_{eff}$  vs  $\eta$  for Various  $\lambda$

For small values of  $\eta$  the effect of the wall thickness is minimal. This quickly changes for larger  $\eta$  which becomes highly dependent on  $\lambda$ . Higher values of  $\lambda$ , and thus larger wall thicknesses, lower resistance, and ultimately lower temperature gradients along the wall height, have the effect of increasing the  $\epsilon_{eff}$ .

### 3.6. Effect of Varying Characteristic Wall Resistance ( $R_{char}$ )

Recall from section 0 that the characteristic wall resistance is the wall's thermal resistance in the  $z$  direction. The relationship between  $\epsilon_{eff}$  and  $R_{char}$  for various values of  $\epsilon_{surf}$  is shown below in Figure 33.

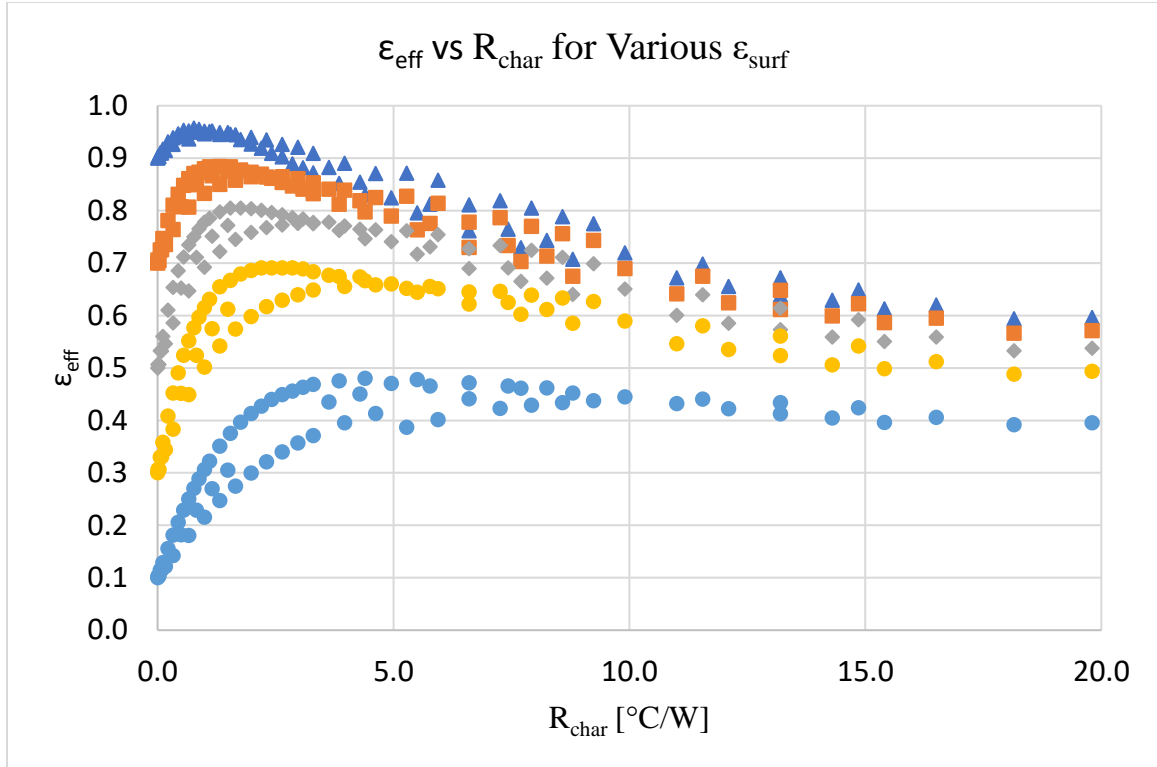


Figure 33:  $\epsilon_{eff}$  vs  $R_{char}$  for Various  $\epsilon_{surf}$

$R_{char}$  is directly proportional to  $H$ , and thus is also proportional to  $\eta$ . It is no surprise then that Figure 33 looks very similarly to the plots of  $\epsilon_{eff}$  vs  $\eta$ . However, a main difference is that  $R_{char}$  combines both the wall height and the wall thickness. The resulting Figure 33 has more variation in the  $\epsilon_{eff}$  value for any given  $R_{char}$ .

### 3.7. Edge Effects

Recall from section 2.4 that the isogrid array model used in this thesis consists of an array of 22x11 cavities. Recall also that the outer edge of the array is assumed to have an emissivity of 0 and thus does not radiate to space. Due to symmetry, we will only look at the  $\epsilon_{eff}$  of cavities from  $0 \leq x \leq 11$  and  $0 \leq y \leq 5$ . This quadrant is representative of the entire array and is shown in green in Figure 34 below.

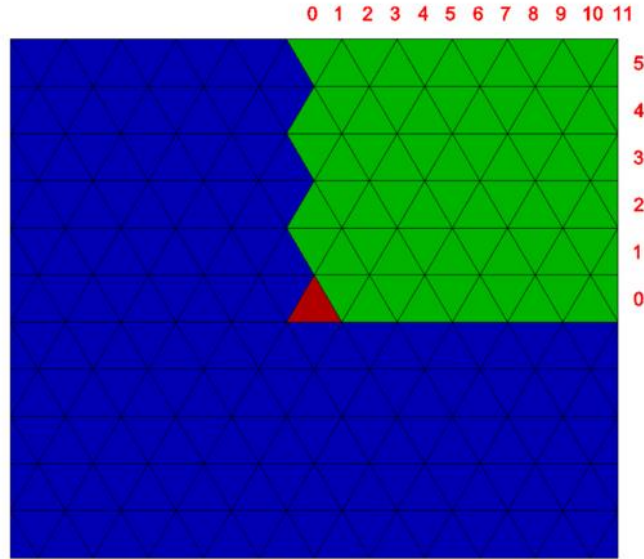


Figure 34: Isogrid Array

In Figure 34 the green cells are the ones whose  $\epsilon_{eff}$  values were calculated and are shown below in Figure 35 and Figure 36. The red cavity at the center is also shown in the Figures below. The edge effect in the x direction is shown below in Figure 35.

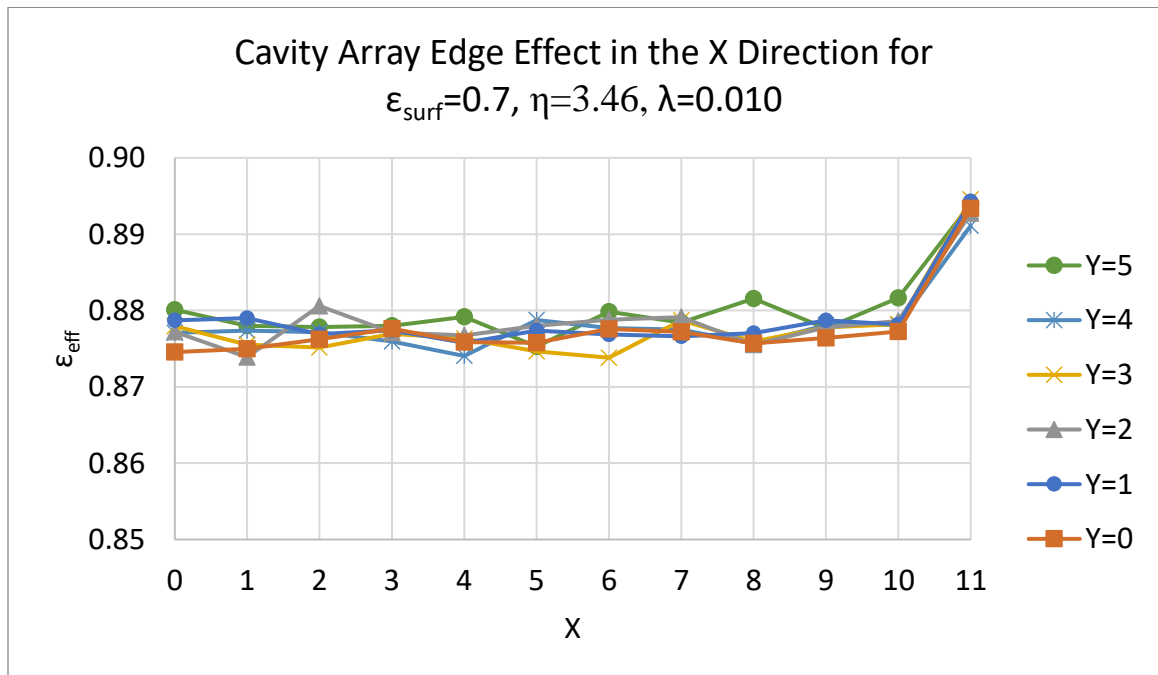


Figure 35: Cavity Array Edge Effect in the X Direction

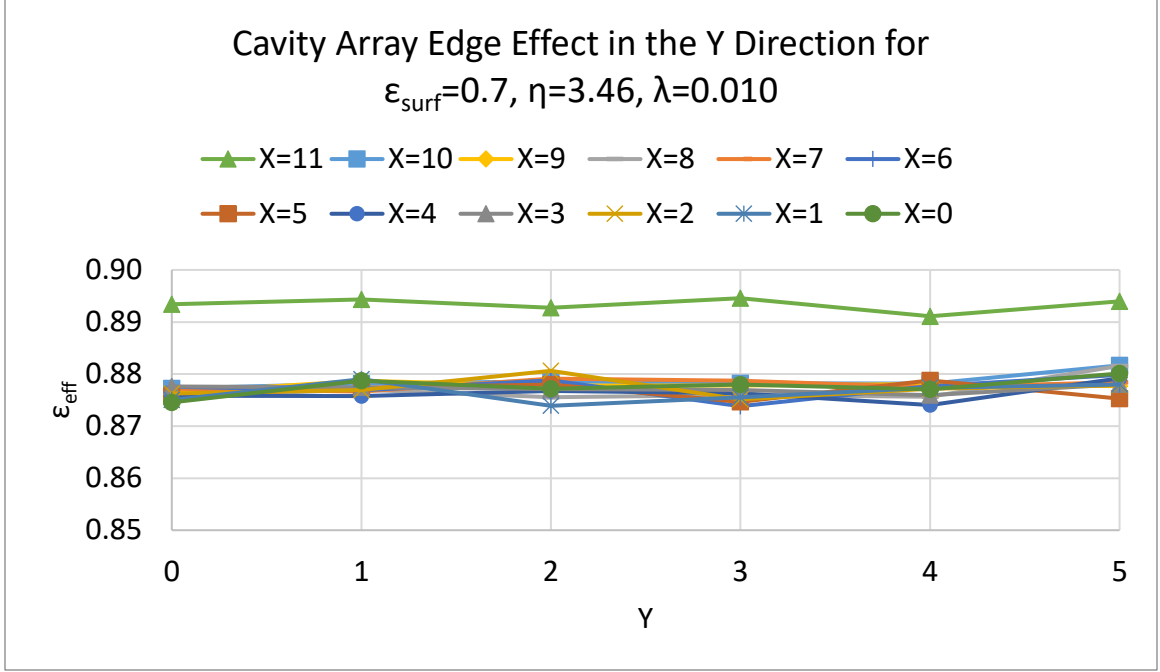


Figure 36: Cavity Array Edge Effect in the Y Direction

In Figure 35 and Figure 36 the  $\epsilon_{eff}$  varies only in the  $x$  direction and not in the  $y$  direction. This is due to the fact that the edge cavities along  $x = 11$  are not equilateral triangles like the other cavities, but rather are right triangles. This geometry has a different  $\eta$  value even though it has the same wall height as the rest of the array. The  $\eta$  for the right triangle is

$$\eta_{right\ triangle} = \frac{\left(\frac{3+\sqrt{3}}{2}\right)LH}{\frac{\sqrt{3}}{8}L^2} = \frac{(12+4\sqrt{3})H}{\sqrt{3}L}$$

$\eta_{equilateral\ triangle} = \frac{12H}{\sqrt{3}L}$ . This larger value of  $\eta$  corresponds to a larger  $\epsilon_{eff}$  for the right triangle edge cavities. The edge cavities at  $y = 5$  are equilateral triangles identical to the rest of the array, so they do not have a larger  $\eta$  value for the given height. The increased  $\epsilon_{eff}$  of the edge cavities is so slight as to be negligible, though the thermal designer should take care to ensure that the overall percentage of edge cavities is small.

### 3.8. Isogrid vs. Other Geometries

The entirety of this thesis has focused on isogrid cavity arrays, which begs the question: what about other geometries besides isogrid? To determine the difference, a single cell model was made for a triangle (isogrid), square (orthogrid), pentagon, hexagon (honeycomb), and a circle. It is well known that pentagons and circles cannot tile a surface and thus cannot readily be used in an array. However, they are examined here to illustrate the effect of various geometric shapes. As seen in Figure 37, the number of sides increases from the triangular isogrid, 3 sides, to a cylinder with an infinite number of sides.

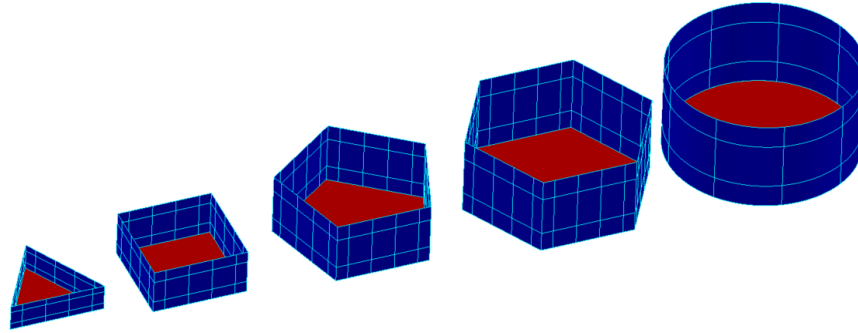


Figure 37: Different Cavity Geometries Tested

The calculation of  $\eta$  for the various geometries is shown in Eqn (30). The dependence of  $\epsilon_{eff}$  on  $\eta$  is shown below in Figure 38.

$$\eta_{triangle} = \frac{3LH}{\sqrt{3}L^2/4}$$

$$\eta_{square} = \frac{4LH}{L^2}$$

$$\eta_{pentagon} = \frac{5LH}{\sqrt{5(5 + 2\sqrt{5})L^2/4}} \quad (30)$$

$$\eta_{hexagon} = \frac{6LH}{3\sqrt{3}L^2/2}$$

$$\eta_{circle} = \frac{2\pi LH}{\pi L^2}$$

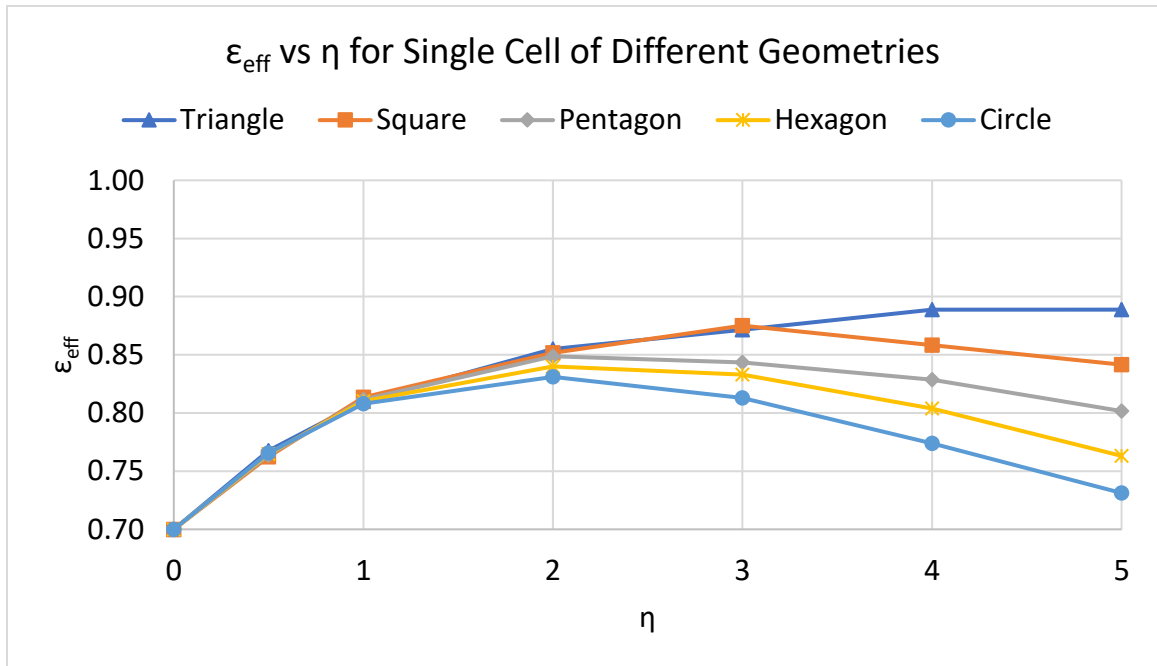


Figure 38:  $\epsilon_{eff}$  vs  $\eta$  for Single Cell of Different Geometries

The results in Figure 38 shows that for small values of  $\eta$  (approximately  $\eta \leq 2$ ) the  $\epsilon_{eff}$  across all geometries are nearly identical. This is because  $H$  is small and the heat rejection

is dominated by the base (as shown in Figure 30). As  $\eta$  increases, the triangle maintains the largest  $\varepsilon_{eff}$ , and the differences between geometries becomes more apparent.

The fact that the triangle maintains the largest  $\varepsilon_{eff}$  means that a radiator designer should always choose isogrid (triangles) over other geometries. For a given amount of heat rejected from the radiator, an isogrid radiator will necessitate the smallest total base area and ultimately the lowest total mass. To explain why this is the case it is prudent to examine the perimeter to area ratio of the geometries in question, shown in Figure 39.

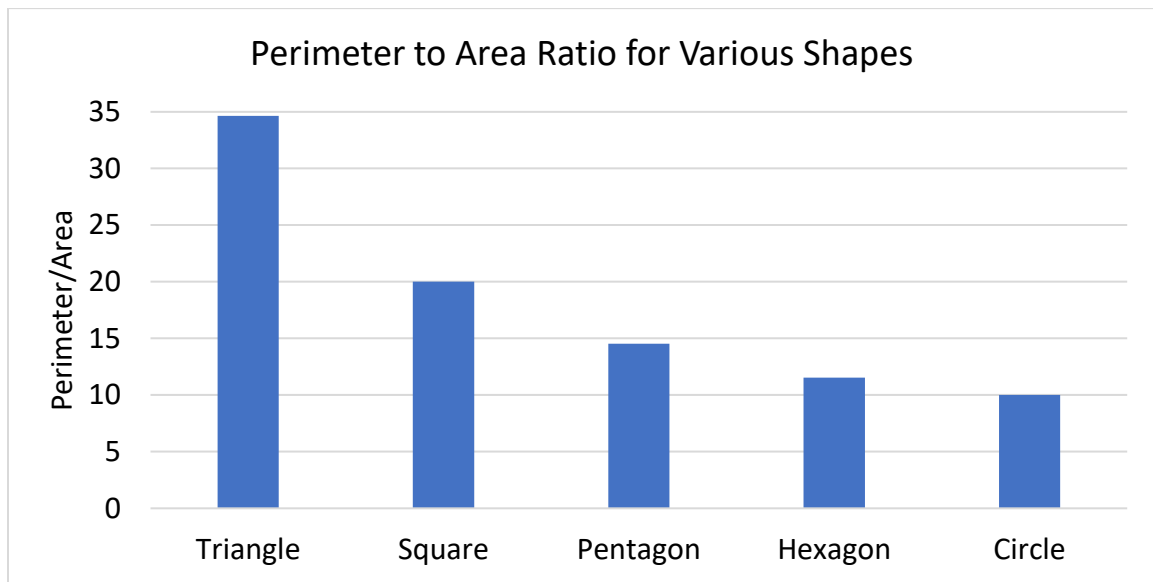


Figure 39: Perimeter to Area Ratio for Various Shapes

Compared to the other shapes, triangles have by far the largest perimeter to area ratio. This implies that for a given value of  $\eta$  a triangle will have the smallest  $H$ , therefore the lowest  $R_{char}$ , therefore the lowest temperature gradients, and correspondingly the highest  $\varepsilon_{eff}$ .

Figure 39 confirms the fact that circles have the largest area for a given perimeter. This is why soap bubbles are circular and not triangular (bubbles optimize for the lowest surface tension which is proportional to perimeter). Of course, circles cannot tile a surface, which is why honeybees make honeycomb from hexagons. They are trying to maximize

the area for a given amount of wax [27]. Perhaps if honeybees were instead trying to maximize the effective emissivity of their hives, honeycomb would look like isogrid!

## Chapter 4: Variable Emissivity Isogrid Radiator Concept

### 4.1. Description

The usefulness of a variable emissivity spacecraft radiator in reducing the required makeup heater power has been discussed in section 1.3.1. The traditional method for achieving variable emissivity is by using a louver as discussed in section 1.3.1.2. Louvers typically vary their emissivity by exposing or covering a high- $\varepsilon$  surface with a low- $\varepsilon$  blade. The blade is actuated by a bi-metallic strip which expands and contracts based on the temperature.

Another method for producing a variable- $\varepsilon$  radiator would be with an isogrid array varying one or more of its parameters as a function of the base temperature  $T_b$ . As was shown in section 3.4, the  $\varepsilon_{eff}$  is highly dependent on the wall height. For this reason, the main parameter to be varied to produce a variable-e isogrid radiator is  $\eta$ . The wall height is perhaps the easiest parameter to dynamically vary, which is the parameter that will be focused on in the following section.

### 4.2. Variable Emissivity Actuation Methods

#### 4.2.1. Variable Base

The first method proposed that could be used to dynamically vary  $\eta$  is by actuating the base up and down the cavity, as shown in Figure 40.

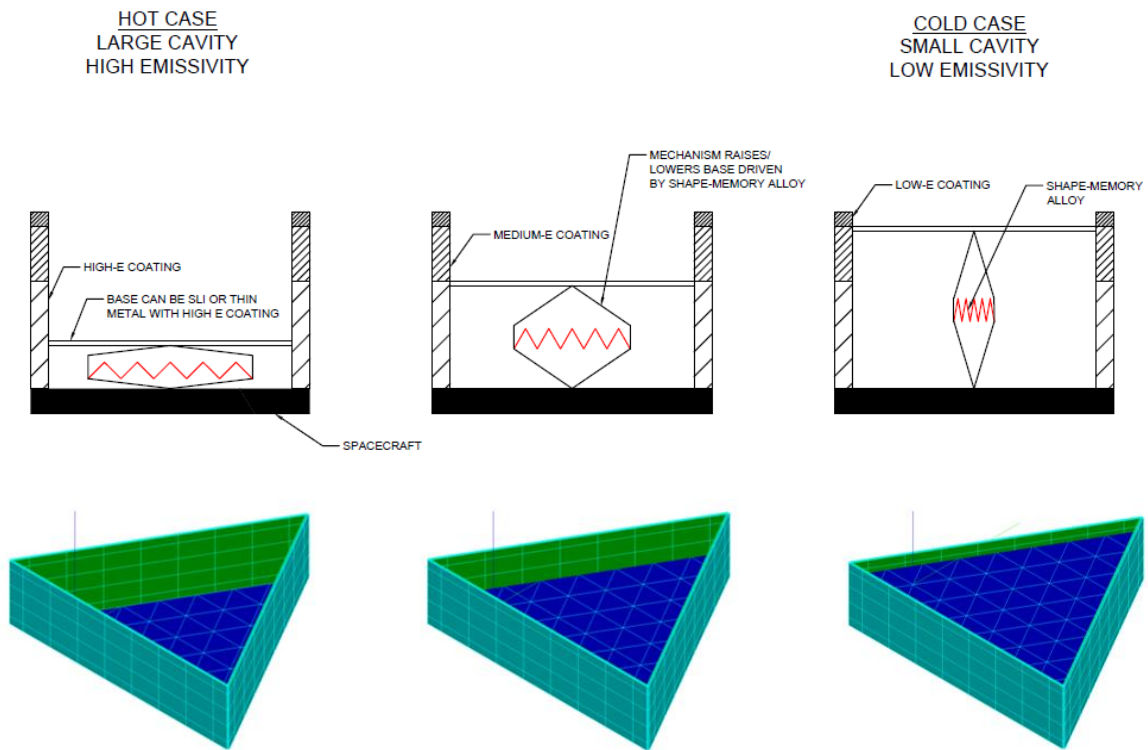


Figure 40: Constant Walls & Variable Base Radiator Schematic

In the hot case the movable base is at the bottom of the cavity, producing the largest possible  $\eta$  and thus the highest possible  $\epsilon_{eff}$ . As the radiator cools, the base moves up the cavity by means of a shape memory alloy or bi-metallic strip. This lowers the  $\eta$  and thus the  $\epsilon_{eff}$ .

A benefit of this method is that the cavity walls do not need to be coated with a single  $\epsilon_{surf}$ . Rather, the top of the walls may be coated with a low- $\epsilon$  coating (lowering the  $\epsilon_{eff}$  in the cold case) and coated with a high- $\epsilon$  finish at the bottom of the cavity (increasing the  $\epsilon_{eff}$  in the hot case). Furthermore, the base itself could be coated with a thermochromic finish which itself varies  $\epsilon_{surf}$  with temperature.

A major challenge with this design is that there necessarily exists a gap between the spacecraft (from which we are trying to reject heat) and the base of the cavity. A flexible thermal strap, or some other method, would need to be employed to thermally couple the spacecraft with the cavity base. The thermal strap increases both the mass and complexity of this actuation scheme.

#### 4.2.2. Variable Walls

The other broad method of varying  $\eta$  with temperature is to keep the base at a fixed location and instead to vary the wall height. This method has the advantage of not needing a thermal strap to couple the spacecraft surface with the base of the cavity.

One way to achieve this physically would be the “propeller” method, shown in Figure 41.

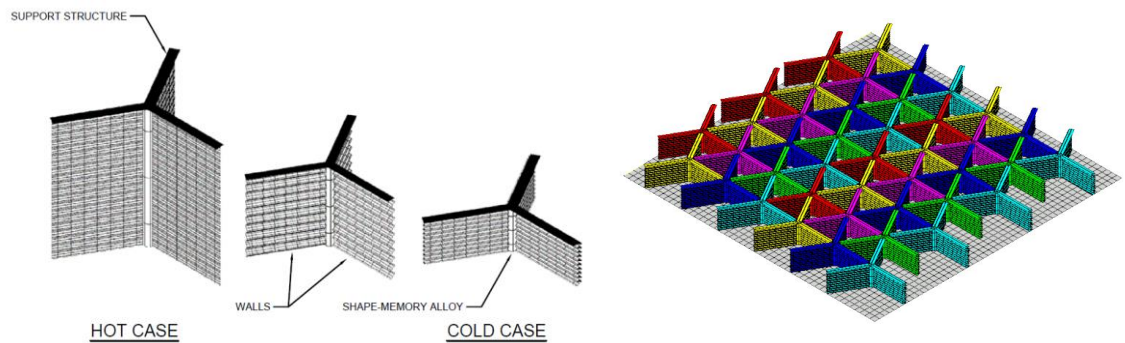


Figure 41: Constant Base and Variable Walls “Propeller” Radiator Schematic

A single mast at the center of the propeller holds 3 “blades” at 120° intervals. Each mast forms the corner of an isogrid cavity, with the blades acting as the walls. The mast changes height with temperature and the cavity walls fold in an accordion fashion.

One challenge with this design is that the walls must be flexible enough to fold up while at the same time having a low enough thermal resistance as to allow enough heat to

be conducted to the top of the cavity. Constructing the walls so that they reliably fold up even after many thousands of cycles would also be a challenge. More analysis of this technique is needed due partially to the fact that in this scheme the  $R_{char}$  is constant even with increasing  $\eta$ . This is because heat must be conducted up the entire height of the wall material even when it is folded up.

## Chapter 5: Summary and Future Work

### 5.1. Conclusion

While the cavity effect has been known and studied for some time, there have been few studies investigating the effective emissivity of nonisothermal cavities. Those that do investigate nonisothermal cavities tend to prescribe a temperature distribution along the wall before solving for the effective emissivity. This study aimed to simultaneously solve for both the temperature profile and for the effective emissivity. Furthermore, most studies investigate a single cylindrical cavity. This thesis investigated an array of isogrid. A cavity within a larger array interacts with its neighbors while, by its nature, a single cavity has no neighbors with which to interact.

This thesis has shown that the effective emissivity of nonisothermal isogrid is primarily dependent on the wall height, wall thickness, wall resistance, and surface emissivity. Increasing the wall height also increases the effective emissivity, but only until the critical wall height ( $\eta_{crit}$ ) is reached. Beyond the critical wall height, the effective emissivity begins to decrease due to the increased thermal resistance up the wall, an increased temperature gradient, and a smaller view factor from the cavity base to space. Further increasing the wall height beyond this critical value has the effect of decreasing the effective emissivity. At a certain point the effective emissivity drops below the surface emissivity of the walls and base (at  $\eta_{equiv}$ ). At the limit, the effective emissivity is hypothesized to asymptotically approach zero as the temperature at the top of the wall approaches that of space.

## 5.2. Future Work

One of the most important next steps which should be taken is validating the thermal model and verifying the results by testing a sample of isogrid in a thermal-vacuum chamber. Validating and correlating the model to test data is needed to verify the results presented in this thesis.

It was shown that increasing the wall thickness directly reduces the thermal resistance up the wall, and correspondingly decreases the temperature gradient. However, there is a possible limit to this increase in the effective emissivity. As the wall thickness increases so too does the area at top of the cavity (at  $z = H$ ). The top of the cavity corresponds to the lowest temperature on the wall, and thus will radiate the least amount of heat and will contribute to lowering the effective emissivity. This effect should be examined by creating a thermal model in which the cavity walls are not assumed to be infinitesimally thin. A model such as this could be used to better characterize the effect of varying the wall thickness in the overall effective emissivity. In making this model one would need to relax the assumption that the temperature is isothermal through the thickness of the walls. More importantly, this model would also account for radiation from the top of the walls which is at the lowest temperature and thus radiates the least.

This thesis only presented results for  $\eta \leq 20$  due to the fine nodalization needed to accurately capture the large non-linear temperature gradients which occur at large  $\eta$  values. It is suggested that  $\eta$  be increased up to at least 1000 to determine if the hypothesis that

$$\lim_{\eta \rightarrow \infty} \varepsilon_{eff} = 0.$$

The edge effect of the cavity array should be better studied. It was shown that the increase in  $\varepsilon_{eff}$  of some of the edge cavities at was due to having a different geometry, a

larger value of  $\eta$ , and correspondingly having a larger  $\varepsilon_{eff}$ . The temperature profile across all of the cavity surfaces (not just surface 1 of the center cavity) should be examined.

In industry it is common to use isogrid to provide structural strength on curved surfaces (such as on cylindrical rocket components). The effective emissivity of isogrid on a curved surface should therefore be examined. If the surface's radius of curvature is large, then the effective emissivity can be assumed to be that of a flat planar isogrid, which was presented in this thesis. The question is: what the largest radius of curvature, in terms of the characteristic length  $L$ , for which the flat plane assumption may be made? What is the effect of having a radius of curvature smaller than this value? If the surface is concave, a cavity will have a view to the rest of the array. This would decrease the overall view factor to space and therefore likely decrease the  $\varepsilon_{eff}$ . A convex surface would have a view factor similar to that of a flat cavity and would not have a view to the rest of the array. In both the concave and convex cases, the cavity's base area (at  $z = 0$ ) and the cavity's opening area (at  $z = H$ ) would no longer be the same due to the cavity being on a curved surface. The effect of these non-equal areas should be examined.

The effect of varying the base temperature should be examined. In the extreme cases, if  $T_b \approx T_{space}$  the temperature gradient on the wall will likely be very small (the wall will be approximately isothermal). If  $T_b \gg T_{space}$  the temperature gradients would likely be much larger, even for the same value of  $\eta$  across both cases. It was shown that moving away from the isothermal ideal case leads to a lower  $\varepsilon_{eff}$ . It is therefore likely that increasing  $T_b$  will increase the temperature gradients and therefore decrease the  $\varepsilon_{eff}$ .

Finally, the directionality of radiative emission from an isogrid cavity opening should be examined. Even if the surfaces composing the cavity are assumed to be diffuse,

emission from the cavity opening could have a strong dependence on the angle. One could imagine that for a large value of  $\eta$  the temperature at the top of the cavity wall would be much lower than the temperature lower on the wall and would thus not radiate as strongly. This could lead to much stronger emission when close to the cavity opening normal, which could quickly decrease with decreasing angle.

## Bibliography

- [1] F. P. Incropera, D. P. Dewitt, T. L. Bergman, and A. S. Lavine, *Fundamentals of Heat and Mass Transfer*, 6th ed. John Wiley & Sons, 2007.
- [2] R. E. Bedford, “Effective Emissivities of Cavity Sources,” in *Theory and Practice of Radiation Thermometry*, D. P. DeWitt and G. D. Nutter, Eds. John Wiley & Sons, Inc., 1988, pp. 653–767.
- [3] A. V. Prokhorov and L. M. Hanssen, “Effective emissivity of a cylindrical cavity with an inclined bottom: I. Isothermal cavity,” *Metrologia*, vol. 46, no. 6, p. 719, 2004, doi: 10.1088/0026-1394/46/6/C01.
- [4] R. E. Bedford and C. K. Ma, “Emissivities of Diffuse Cavities -Isothermal and Nonisothermal Double Cones,” *J Opt Soc Am*, vol. 66, no. 7, pp. 724–730, 1976, doi: 10.1364/josa.66.000724.
- [5] D. G. Gilmore *et al.*, *Spacecraft Thermal Control Handbook Volume I: Fundamental Technologies*, 2nd ed. The Aerospace Press, 2002.
- [6] J. L. Champion, R. Osiander, and T. D. Swanson, “MEMS Louvers for Thermal Control,” 1998.
- [7] J. Triolo, “Thermal Coatings Seminar Series Training Part 1: Properties of Thermal Coatings,” 2015.
- [8] R. N. Miyake, “Spacecraft Design Thermal Control Subsystem.” Jet Propulsion Laboratory, 2008.
- [9] N. Athanasopoulos and N. J. Siakavellas, “Programmable thermal emissivity structures based on bioinspired self-shape materials,” *Sci. Rep.*, vol. 5, pp. 1–14, 2015, doi: 10.1038/srep17682.
- [10] N. Athanasopoulos and N. J. Siakavellas, “Smart patterned surfaces with programmable thermal emissivity and their design through combinatorial strategies,” *Sci. Rep.*, vol. 7, no. 1, pp. 1–16, 2017, doi: 10.1038/s41598-017-13132-6.
- [11] T. D. Swanson, “MEMS DEVICE FOR SPACECRAFT THERMAL CONTROL APPLICATIONS,” 6538796B1, 2003.
- [12] R. B. Mulford, M. R. Jones, and B. D. Iverson, “Heat transfer, efficiency and turn-down ratio of a dynamic radiative heat exchanger,” *Int. J. Heat Mass Transf.*, vol. 143, 2019, doi: 10.1016/j.ijheatmasstransfer.2019.118441.
- [13] L. Keeseey, “NASA’s New Shape-Shifting Radiator Inspired by Origami,” *NASA Goddard Space Flight Center*, 2017. <https://www.nasa.gov/feature/goddard/2017/nasa-s-new-shape-shifting-radiator-inspired-by-origami>.
- [14] R. M. Fowler, L. L. Howell, and S. P. Magleby, “Compliant space mechanisms: A new frontier for compliant mechanisms,” *Mech. Sci.*, vol. 2, no. 2, pp. 205–215, 2011, doi: 10.5194/ms-2-205-2011.
- [15] H. Nagano, Y. Nagasaka, and A. Ohnishi, “Simple deployable radiator with autonomous thermal control function,” *J. Thermophys. Heat Transf.*, vol. 20, no. 4, pp. 856–864, 2006, doi: 10.2514/1.17988.
- [16] C. Bertagne, P. Walgren, L. Erickson, R. Sheth, J. Whitcomb, and D. Hartl, “Coupled behavior of shape memory alloy-based morphing spacecraft radiators: Experimental assessment and analysis,” *Smart Mater. Struct.*, vol. 27, no. 6, 2018,

doi: 10.1088/1361-665X/aabbe8.

- [17] H. Demiryont and D. Moorehead, “Electrochromic emissivity modulator for spacecraft thermal management,” *Sol. Energy Mater. Sol. Cells*, vol. 93, no. 12, pp. 2075–2078, 2009, doi: 10.1016/j.solmat.2009.02.025.
- [18] NASA, “NASA Telescope Named For ‘Mother of Hubble’ Nancy Grace Roman.” <https://www.nasa.gov/press-release/nasa-telescope-named-for-mother-of-hubble-nancy-grace-roman>.
- [19] NASA, “Nancy Grace Roman Space Telescope,” *NASA Goddard Space Flight Center*. <https://roman.gsfc.nasa.gov/observatory.html>.
- [20] H. L. Peabody, “Tracking Critical Thermal Metrics throughout the Life Cycle of a Large Observatory Thermal Model,” 2020.
- [21] NASA, “WIDE FIELD INSTRUMENT.” [https://roman.gsfc.nasa.gov/wide\\_field\\_instrument.html](https://roman.gsfc.nasa.gov/wide_field_instrument.html).
- [22] NASA, “CORONAGRAPH.” <https://roman.gsfc.nasa.gov/coronagraph.html>.
- [23] J. R. Howell, M. P. Menguc, and R. Siegel, *Thermal Radiation Heat Transfer*, 6th ed. Boca Raton, FL: CRC Press, 2016.
- [24] F. O. Bartell, “Cavity Emissivities Greater Than One,” *Thermosense VII Therm. Infrared Sens. Diagnostics Control*, vol. 0520, no. March 1985, p. 34, 1985, doi: 10.1117/12.946127.
- [25] T. D. Panczak, S. G. Ring, M. J. Welch, D. Johnson, B. A. Cullimore, and D. P. Bell, *Thermal Desktop User’s Manual*, 6.0. C&R Technologies, Inc., 2017.
- [26] B. A. Cullimore, S. G. Ring, and D. A. Johnson, *SINDA/FLUINT User’s Manual*, 5.5. C&R Technologies, Inc, 2011.
- [27] T. C. Hales, “The Honeycomb Conjecture,” *Discret. Comput. Geom.*, vol. 25, no. 1, pp. 1–22, 2001, doi: 10.1007/s004540010071.

